ACCEPTED MANUSCRIPT

Three-Dimensional Numerical Investigation of Ground Response and Stability of Gate Roadways and Pillars in Longwall Mining

Hasan Ghasemzadeh[1a], Hasan Madani[*1], Farhang Sereshki[2b], Sajjad Afraei[1c]

[1]*Department of Mining Engineering, Amirkabir University of Technology, Tehran, Iran*
[2]*Faculty of Mining, Petroleum and Geophysics, Shahrood University of Technology, Shahrood, Iran*

Abstract. Ground stability around gate roadways and panel pillars is strongly influenced by stress redistribution during progressive longwall extraction. This study evaluates the stability response of the C1W4 panel in the Parvadeh IV coal mine using three-dimensional FLAC3D simulations, focusing on the effect of pillar width on roadway and pillar performance. Five pillar-width alternatives were assessed using an integrated stability framework considering stress redistribution, deformation, critical shear strain, plastic-zone development, support response, and stress–strength ratio (SSR). The results show that narrower pillars experience higher stress concentration, greater deformation, extensive plastic yielding, and reduced SSR values. The 4 m pillar exceeded the critical shear strain threshold and exhibited unstable behavior, while the 6 m pillar showed insufficient mechanical reliability under the investigated loading conditions. The 8 m pillar represented a transitional condition with limited stability margin. In contrast, the 10 and 12 m pillars maintained higher SSR values, controlled deformation, and localized plasticity mainly at their peripheral zones. The numerical model was validated using field extensometer measurements, showing satisfactory agreement between simulated and measured roof displacements with an RMSE of 1.60 mm and a MAPE of 22.17%. Among the evaluated alternatives, the 10 m pillar provided a mechanically stable solution under the geological and loading conditions of the studied panel. However, the transition between marginal and stable behavior occurs between 8 and 10 m, requiring further investigation with smaller pillar-width increments. The proposed multi-criteria numerical framework provides a systematic approach for assessing roadway and pillar stability in longwall coal mining.

Keywords: Longwall extraction; Coal pillar stability; Gate roadway behavior; Stress redistribution; Three-dimensional numerical modeling

1. Introduction

Longwall extraction is widely recognized as an efficient method for underground coal production, yet the progressive caving associated with this method creates challenging ground-control conditions around gate roadways and panel pillars. As the longwall face moves forward, roof failure and gob development progressively modify the original stress field and transfer loads toward the pillars and surrounding strata. The resulting abutment stress concentration can promote progressive pillar yielding, floor heave, excessive loading

[*]Corresponding author, *Assistant Professor*, E-mail: madani.hasan.aut@gmail.com
[a] *Ph. D Candidate*, E-mail: h.ghasemzadeh@aut.ac.ir
[b] Professor, E-mail: f.sereshki@gmail.com
[c] Assistant Professor, E-mail: Sajjad.Afraei@aut.ac.ir

of support systems, and deterioration of coal-pillar integrity. Consequently, controlling the stability of gate roadways throughout the extraction process is fundamental to maintaining safe and continuous mine operation [1-4].

The geomechanical conditions encountered by gate entries in advancing longwall operations are continuously modified as the face progresses. The combined effects of caving-induced load transfer, pillar dimensions, and support response can therefore produce highly variable ground behavior along the extraction sequence. Among the design parameters, pillar width has a particularly important influence on the load-carrying capacity of the coal mass, the extent of yielding, and the magnitude of surrounding deformation. Although reducing pillar width may improve coal recovery, undersized pillars can be subjected to severe failure and increased permeability. Conversely, unnecessarily large pillars may improve stability at the expense of extraction efficiency. The selection of an appropriate pillar dimension consequently requires a balance between geotechnical performance and production considerations [5,6].

The role of stress conditions and excavation geometry in underground stability has been recognized since the early numerical studies of underground openings, which demonstrated the sensitivity of instability patterns to excavation orientation and in-situ stress [7]. Further investigations examined the response of haulage entries and jointed rock masses to longwall-induced loading under different stress conditions [8,9]. The geomechanical consequences of mining beneath aquifers were also investigated [10], while the principal concepts and practices associated with ground control in longwall operations were systematically summarized in established ground-control literature [11].

As mining has progressed to greater depths and larger panel dimensions, increasing attention has been directed toward the redistribution of stress around pillars and the resulting ground response. Studies of chain and barrier pillars have shown that high abutment stresses commonly develop close to pillar boundaries and change position as the longwall face advances [12,13]. In deep underground mines, high in-situ stresses can substantially increase deformation and failure around gate entries [14]. Similarly, elevated shear stresses in roof strata and roadway intersections have been identified as important contributors to instability [15]. Other investigations have documented progressive decreases in the safety factor of pillars and bleeder entries located adjacent to gob areas during caving [16]. Analytical approaches have also been developed to describe the temporal development of stress concentration and distressed regions within coal pillars [17].

Since approximately 2017, numerical investigations have increasingly addressed the coupled behavior of the gob, pillars, and gate-roadway system rather than treating these components independently. Finite-difference analyses have been used to examine the effects of unilateral gob loading and great mining depth on gateroad arrangements [18], while extraction-induced tensile failure around ventilation tunnels has also been investigated [19]. Numerical studies have further clarified the evolution of roof loading during successive stages of face advance and its implications for support performance [20]. The spacing of steel sets has been optimized in an effort to achieve an appropriate balance between ground-control requirements and economic efficiency [21]. FLAC3D-based analyses have examined the influence of seam inclination on stress and displacement distributions [22], and the behavior of steel sets subjected to high pressure and complex geological conditions has been evaluated [23]. Other studies have investigated the effects of panel height on roof-loading intervals [24] and proposed approaches for controlling floor heave in coal-mine tunnels tunnels [25].

Recent research has placed greater emphasis on three-dimensional numerical simulation and the interaction of multiple components under increasingly complex extraction conditions. The effects of simultaneous extraction of neighboring panels on maingate stability have been examined numerically [26], while alternative secondary gateroad support arrangements have been developed for thin coal seams adjacent to gob areas [27]. Progressive rock-mass deformation and shear fracturing near active longwall faces have also been investigated [28]. Field-calibrated numerical models have subsequently been employed to assess support-system behavior under actual mining conditions [29]. Comparative studies have indicated that appropriately developed numerical models can reproduce field observations more closely than simplified analytical or empirical approaches, particularly for deep-cover mining environments [30]. Other investigations have considered the influence of seam inclination [31], pillar damage under combined gravitational and tectonic stresses [32],

ACCEPTED MANUSCRIPT

lateral stress redistribution during progressive extraction [33], the reuse of headgate and tailgate entries [34], barrier-pillar dimension optimization [35], stress transfer toward overlying coal seams [36], and the control of squeezing ground conditions through combined support systems in mechanized coal mines [37].

Despite this extensive body of research, the assessment of pillar and roadway stability is often based on a limited number of individual indicators. Empirical pillar-design methods can provide useful initial estimates, but their ability to account for local geological characteristics and the changing loading conditions associated with progressive caving is restricted. Analytical solutions similarly require simplifying assumptions regarding stress distribution and are generally unable to reproduce the three-dimensional interaction between the excavation, pillars, surrounding strata, and gob. Numerical modeling offers greater flexibility for representing these coupled processes; nevertheless, a considerable proportion of existing numerical studies emphasizes individual measures of stability, such as displacement, plastic-zone development, or stress–strength ratio, rather than considering their combined implications. In particular, the simultaneous interpretation of stress redistribution, deformation, failure development, support response, and SSR for pillar-dimension selection under a continuously advancing face remains insufficiently developed.

Another important limitation concerns the connection between numerical predictions and actual field behavior. Even sophisticated numerical models may provide uncertain engineering interpretations when their predictions are not evaluated against independent monitoring observations. A practical design methodology should therefore not only incorporate several complementary mechanical indicators but also establish an explicit engineering basis for interpreting them and should be supported by field measurements wherever possible. Such an approach is particularly important when the objective is to distinguish between marginally stable and adequately stable pillar configurations and to determine an appropriate design range under site-specific loading conditions.

The Parvadeh IV coal mine in the Tabas coalfield of central Iran represents a suitable case for investigating these issues. The mine employs longwall extraction in relatively thin coal seams under moderate overburden depth. Within the C1W4 panel, continued face advance and associated caving progressively alter the stress environment around the maingate and its panel pillars. Field observations have included localized pillar spalling and floor deformation, indicating that the interaction between pillar geometry, surrounding strata, and roadway support requires detailed assessment.

Accordingly, this study develops a three-dimensional numerical approach for examining the effect of pillar width on the stability of the maingate roadway and panel pillars during progressive longwall extraction. The assessment combines six complementary aspects of ground response: stress redistribution, displacement, critical shear strain, plastic-zone development, support-system performance, and the stress–strength ratio (SSR). Rather than relying on a single stability measure, the proposed evaluation considers the most restrictive response as the controlling condition for engineering interpretation. In addition, numerical results are compared with extensometer observations obtained from the operating longwall panel to assess the capability of the model to reproduce actual roof deformation.

The specific objective is to evaluate five pillar-width alternatives under successive stages of face advance and to establish the corresponding changes in stress, deformation, yielding, support demand, and SSR. Critical shear strain is evaluated according to Sakurai's criterion [38], while the other indicators are interpreted in combination to characterize the overall stability condition. This approach is intended to identify a pillar-width range that provides adequate mechanical performance without imposing unnecessary limitations on coal recovery.

By integrating three-dimensional numerical simulation, multiple stability indicators, and field-based validation, the study provides a performance-oriented procedure for assessing pillar dimensions and gate-roadway stability in advancing longwall operations. The methodology is developed for the geological and loading conditions of the C1W4 panel but can also provide a basis for similar underground coal mines where progressive caving, stress redistribution, and ground-control requirements interact.

2. Description of the Study Area

The Parvadeh coalfield is situated in central Iran, approximately 85 km south of Tabas, and extends over

ACCEPTED MANUSCRIPT

an area of nearly 1200 km². The field constitutes an important structurally controlled coal-bearing region and is divided into five principal sectors: Parvadeh 1, Parvadeh 2, Parvadeh 3, Parvadeh 4, and the Eastern sector. Major faults separate several of these sectors and have an important influence on the regional stress regime as well as on mine development and extraction strategies (Fig. 1) [39,40].

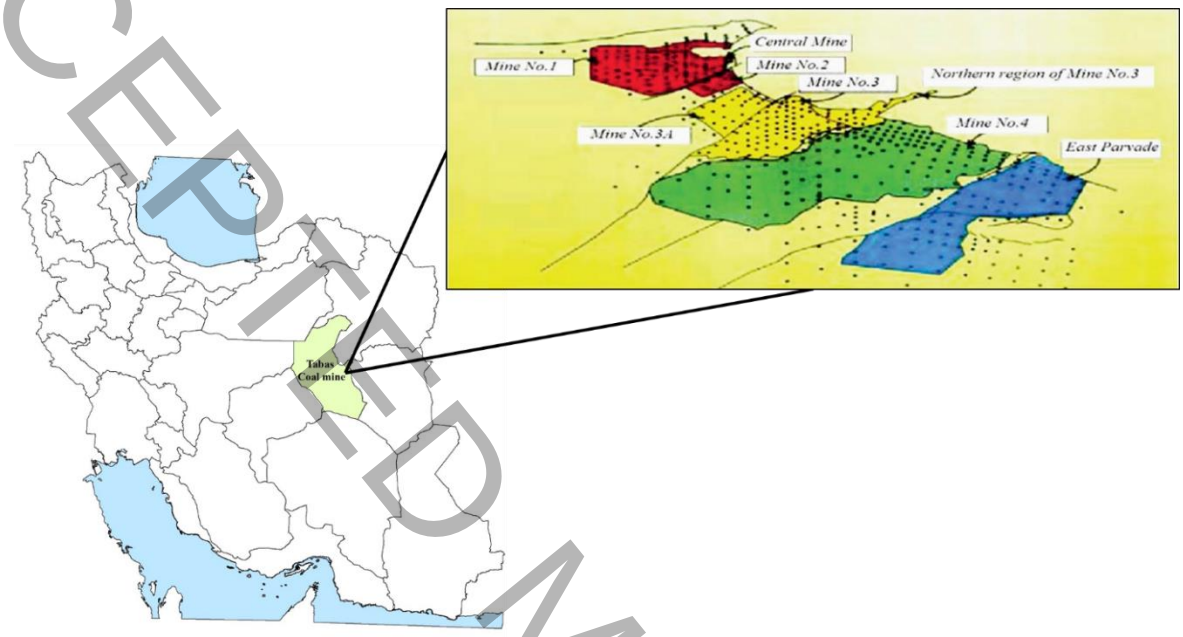

Fig. 1 Location of the Parvadeh coal mines and the separating faults

The sedimentary sequence of the Parvadeh Formation consists mainly of siltstone, mudstone, sandstone, and coal, forming a predominantly layered stratigraphic succession. The exploitable coal seams are relatively thin, with thicknesses of approximately 0.9–1.1 m, while their dip generally varies from 0 to 2°. The relatively small seam inclination permits the strata to be treated as approximately horizontal in the numerical analysis. This simplification reduces model complexity while retaining the principal mechanisms associated with mining-induced stress redistribution.

Parvadeh 4 contains approximately 41% of the coal resources of the entire coalfield and represents its largest reserve block. Three mineable seams, namely C1, C2, and B1, have been identified within this sector. The C1 seam is extracted from the western part of the sector using an advancing longwall system, whereas retreating longwall extraction is applied to the B1 and C2 seams in the eastern part [39,40].

The C1W4 panel was selected as the case study because it was undergoing active longwall extraction at the time of the investigation. Approximately 300 m of the panel had been extracted, representing about 40% of the planned panel length. The panel dimensions are designed within a range of approximately 400–900 m in length and 80–150 m in width, with an overburden thickness of about 150 m at the investigated operating depth. The study section corresponds to one of the deepest active mining conditions in Parvadeh IV.

The numerical analysis was designed to investigate the local mechanical response of the maingate-side pillar and surrounding roadway during progressive face advance rather than to reproduce the complete geometry of the C1W4 panel. Accordingly, the model extent was defined according to the zone affected by mining-induced stress changes and the availability of field monitoring data. The maingate-side pillar was selected because multi-point extensometer measurements were available at this location, providing an independent basis for calibration and subsequent validation of the numerical predictions. At the investigated stage of extraction, the pillar side facing the mined-out area was subjected to the influence of the caved/gob zone, whereas its opposite side remained connected to intact coal ahead of the advancing face.

ACCEPTED MANUSCRIPT

The maingate and tailgate entries have horseshoe-shaped cross-sections, each approximately 3 m wide and 2 m high. Because of the thin seam geometry and economic considerations, conventional longwall extraction accompanied by stepwise caving remains the principal mining practice. Ground support includes arched steel sets and shotcrete, which are used to maintain roadway integrity during extraction [39,40]. The general mine configuration and the extraction condition of the C1W4 panel during the investigation are presented in Fig. 2. This figure is intended to illustrate the actual mining context and panel configuration and should not be interpreted as a representation of the numerical model boundaries.

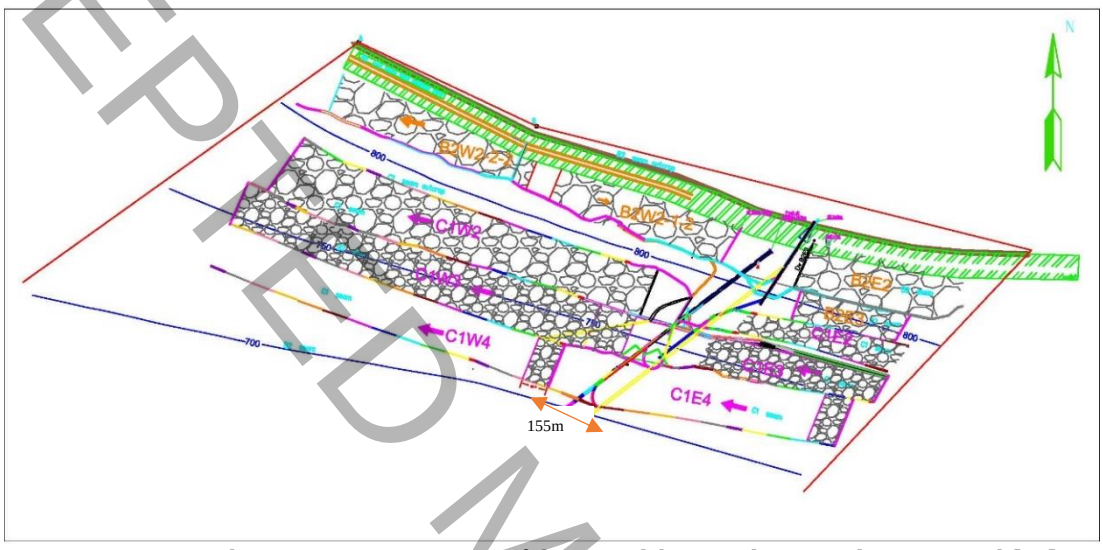

Fig. 2 Layout and current extraction status of the Parvadeh IV coal mine and C1W4 panel [40]

The geotechnical environment of Parvadeh IV is characterized by several interacting ground-control issues. These include stress concentration around panel pillars, the mechanical response of the gob generated by roof caving, and the interaction between adjacent roadways and extracted areas. Spontaneous combustion is also an important operational issue in the mine; however, it is outside the primary scope of the present investigation, which is restricted to the mechanical stability of the roadway–pillar system. The combination of panel geometry, progressive extraction, and pillar arrangement makes the site suitable for examining the response of different pillar dimensions and their interaction with roadway support.

The existing mining configuration comprises a series of longwall panels intended for progressive extraction of the Parvadeh IV sector. Consequently, the sequence of panel extraction and the management of caved areas influence the evolution of the surrounding stress field. These site-specific characteristics, together with the availability of field deformation measurements, make C1W4 a suitable case for evaluating pillar and roadway behavior during advancing longwall extraction.

Overall, the geological setting, thin coal seam, moderate overburden depth, mining geometry, and active extraction conditions provide a representative engineering environment for investigating ground response in longwall coal mining. The C1W4 panel consequently offers an appropriate field case for numerical assessment of pillar stability, roadway deformation, and pillar–support interaction, with the additional advantage of being supported by field-based monitoring data.

3. Numerical Modeling (Methodology)

A three-dimensional FLAC3D model was established for the C1W4 longwall panel at the Parvadeh IV coal mine to investigate the mechanical response and stability of the gate roadways and panel pillars during progressive extraction and caving. Since no major geological discontinuities were identified within the

ACCEPTED MANUSCRIPT

investigated panel, the surrounding rock mass was represented as a continuous medium. This assumption permits the finite-volume formulation implemented in FLAC3D to be applied to the study domain, where the governing equilibrium relations for stress, displacement, and energy are solved explicitly over a discretized assembly of volumetric zones [41].

The overall numerical procedure is illustrated in Fig. 3. The modeling sequence began with the definition of the model geometry, followed by spatial discretization and assignment of the required material properties. Initial in-situ stress conditions were then established before excavating the maingate and tailgate roadways. The subsequent stages included representation of roof relaxation, implementation of the roadway support systems, and stepwise simulation of longwall advance and the associated development and mechanical response of the gob (caved zone).

In addition to the conventional deformation and stress-based outputs, the stress–strength ratio (SSR) available in FLAC3D was employed as an indicator of the proximity of the modeled rock mass to its failure condition. The SSR is defined within the numerical analysis in terms of the relationship between the strength available in the material and the stress state generated around the excavation and pillar boundaries. The strength term is determined from the constitutive-model parameters, including cohesion, friction angle, and tensile strength, whereas the corresponding stress state is obtained from the mining-induced stress field calculated during the simulation. Consequently, the spatial distribution of SSR can be used to identify regions where the computed stress state approaches or exceeds the available material strength and, therefore, to evaluate the relative stability of the roadway and pillar system.

ACCEPTED MANUSCRIPT

ACCEPTED MANUSCRIPT

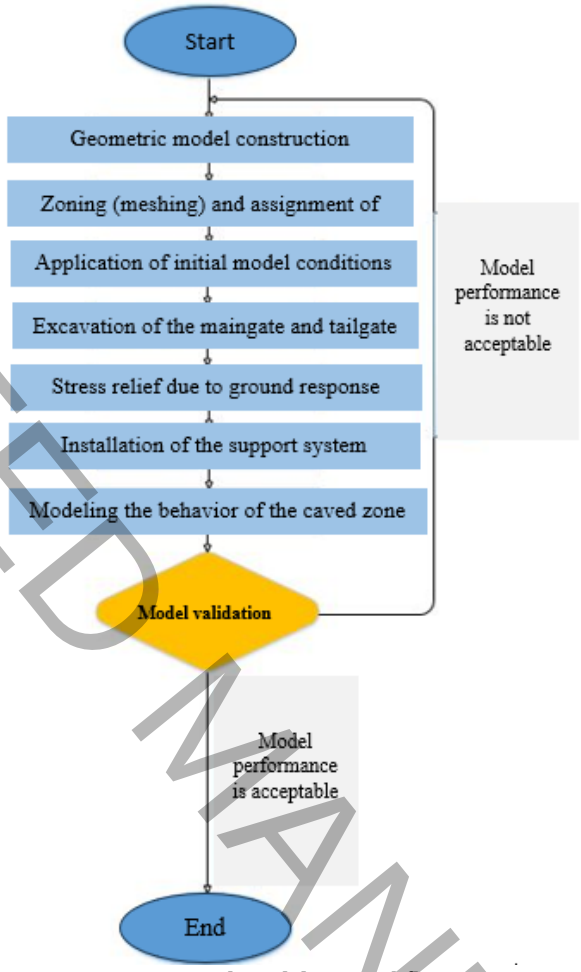

Fig. 3 Numerical modeling workflow

3.1. Model Geometry and Boundary Conditions

The numerical domain was constructed to represent an 80 m-wide active section of the C1W4 longwall panel, with a modeled length of 146 m and a coal-seam thickness of 1 m. Five pillar-width configurations, ranging from 4 to 12 m, were considered. The maingate and tailgate entries were represented by horseshoe-shaped excavations with a width of 3 m and a height of 2 m.

Although the total panel length along the strike direction is within the range of 400–900 m, the 146 m length adopted in the numerical model represents only the actively extracted segment associated with the field monitoring period. In contrast, the 80 m model width corresponds to the actual face width of the C1W4 panel. Thus, the modeled geometry should not be interpreted as the complete longwall panel. The longitudinal extent was selected to encompass the mining-induced influence region around the investigated maingate-side pillar while remaining consistent with the period for which extensometer measurements were available. This localized modeling strategy avoids unnecessary enlargement of the computational domain while retaining the principal stress redistribution and deformation mechanisms relevant to the stability assessment.

The vertical model extent was defined independently of the approximately 150 m overburden thickness at the current mining depth. Geological evidence and observations of caving behavior in Parvadeh IV indicate

that the dominant deformation and stress changes associated with longwall extraction occur within the strata immediately surrounding the excavations. Accordingly, a 26 m thick rock-mass section was explicitly incorporated into the model, including the 1 m coal seam and the immediate roof strata involved directly in the failure and deformation processes. The mechanical contribution of the overlying sandstone and mudstone layers outside this explicitly modeled zone was represented through an equivalent vertical stress of 4 MPa applied at the upper boundary. This treatment provides the modeled strata with the required overburden loading without introducing the full 150 m overlying sequence into the computational domain.

The upper surface was therefore loaded with a uniform vertical stress of 4 MPa to represent the weight of the remaining overburden. The initial horizontal stress was established using a horizontal-to-vertical stress ratio of $K_0 = 1.0$. Because direct measurements of the horizontal in-situ stress were unavailable for the investigated panel, this value was adopted as a first-order approximation of an approximately isotropic initial stress state. The assumption is intended primarily to provide a consistent reference stress condition for comparing the mechanical response of the different pillar-width alternatives, rather than to reproduce the absolute regional stress field. Normal displacement was constrained at the floor and lateral boundaries.

The C1W4 seam has a dip of only 0–2°. The small inclination was consequently neglected and the coal seam and surrounding strata were represented as approximately horizontal. This geometric simplification reduces model complexity while retaining the principal mechanisms of mining-induced stress redistribution.

Longwall extraction was represented by successive 10 m face-advance increments. Five stages of caving were simulated, corresponding to cumulative extraction distances of 10, 20, 30, 40, and 50 m. This staged procedure was adopted to reproduce the progressive development of the caved zone and the associated evolution of the stress and deformation fields around the pillars and gate roadways.

Approximately 30 numerical simulations were performed to investigate the response of the five pillar-width configurations under progressive extraction. The corresponding pillar widths were 4, 6, 8, 10, and 12 m, while the modeled gob lengths varied from 94 to 108 m as a function of pillar width. Extraction advances of 10–50 m were considered in the five caving stages. The principal geometric parameters and the number of analyzed models are summarized in Table 1.

Table 1. Geometric specifications and number of developed models

Model No.	Pillar width (m)	Pillar transverse coordinates, x (m)	Transverse coordinates of the caving-zone boundary, x (m)	Gob length (m)	Tunnel dimensions (m)	Caving step (m)	Number of caving stages analyzed
1	4*10*1	Pillar1: 15-19 Pillar2: 127-131	19-127	108	3*2	10	5
2	6*10*1	Pillar1: 15-21 Pillar2: 125-131	21-125	104	3*2	10	5
3	8*10*1	Pillar1: 15-23 Pillar2: 123-131	23-123	100	3*2	10	5
4	10*10*1	Pillar1: 15-25 Pillar2: 121-131	25-121	96	3*2	10	5
5	12*10*1	Pillar1: 15-27 Pillar2: 119-131	27-119	94	3*2	10	5

Figure 2 shows the general mining configuration and the extraction status of C1W4 at the time of investigation; it is not intended to define the numerical model boundaries. The modeled pillar represents the

ACCEPTED MANUSCRIPT

ACCEPTED MANUSCRIPT

maingate-side pillar under an advancing-face condition. Its mined-out side is subjected to the influence of the previously extracted and caved region, whereas the opposite side remains connected to intact coal in front of the advancing face. The pillar was selected for analysis because multi-point extensometer observations were available at the corresponding maingate location, enabling the numerical results to be calibrated and subsequently compared with field measurements. Accordingly, the pillar was modeled as part of an active longwall system rather than as an isolated barrier pillar bounded by gob on both sides.

The previously extracted C1E4 panel was excluded from the explicit numerical domain. Its center-to-center separation from C1W4 is approximately 155 m, and an intact coal barrier remains between the main entries and the adjacent panel. This intervening coal zone provides a substantial separation between the two extraction areas and limits their direct mechanical interaction within the near-field region considered in this study. On this basis, the direct influence of C1E4 on the local stress redistribution and deformation of the C1W4 roadway–pillar system was not explicitly represented. Regional stress effects were instead incorporated through the prescribed initial and boundary stress conditions.

This modeling choice was made in accordance with the primary objective of the study, which is to compare the local mechanical response of different pillar widths under the same progressive extraction conditions. A larger-scale model incorporating C1E4 could be used in future work to investigate possible far-field interactions between adjacent panels and their influence on the regional stress field.

3.2. Material Properties and Constitutive Models

Different constitutive formulations were assigned to the intact strata and the caved material to reproduce their distinct mechanical responses during longwall extraction. The Mohr–Coulomb model was used for the coal seam and surrounding intact rock, whereas the double-yield formulation was employed for the gob to account for its compressible and irreversible compaction. The mechanical parameters of the modeled materials were established from field investigations, laboratory tests performed on borehole samples obtained from the Parvadeh IV mine, and geological characterization of the rock mass using the Geological Strength Index (GSI) method. Based on field descriptions and observed rock-mass conditions, a GSI value of approximately 40 was assigned to the surrounding strata. Laboratory uniaxial compression tests yielded an intact coal UCS of approximately 16 MPa, which was used in defining the strength characteristics of the coal. Comparable material parameters have also been reported in previous numerical investigations of the same mining area [26].

The geological sequence of the Parvadeh Formation also contains sandstone and mudstone; however, these units were not explicitly introduced as separate material zones in the present model. Their location outside the principal near-field region governing the local roadway–pillar response made their explicit representation unnecessary for the objectives of this study. Instead, their mechanical contribution was incorporated through the equivalent overburden loading imposed at the upper model boundary. Consequently, Table 2 contains the properties of the two materials directly represented in the numerical domain, namely siltstone and coal.

The mechanical parameters assigned to these materials comprise cohesion, internal friction angle, tensile strength, dilation angle, bulk modulus, shear modulus, Young's modulus, Poisson's ratio, and density. The elastic parameters were internally checked for consistency by deriving Young's modulus and Poisson's ratio from the bulk and shear moduli used in FLAC3D. These parameters were obtained from ($E=9KG/(3K+G)$) and ($\boldsymbol{\nu}=(3K-2G)/[2(3K+G)]$), respectively. For the siltstone, bulk and shear moduli of 1.7 GPa and 0.9 GPa give a Young's modulus of 2.30 GPa and a Poisson's ratio of 0.28. For coal, the corresponding values of 2.11 GPa and 1.26 GPa result in a Young's modulus of 3.13 GPa and a Poisson's ratio of 0.24.

Table 2. Mechanical properties of coal and surrounding rock materials used in the numerical model

Rock type	Cohesion (MPa)	Internal friction angle (°)	Tensile strength (MPa)	Dilation Angle (°)	Bulk Modulus (GPa)	Shear modulus (GPa)	Young's Modulus (GPa)	Poisson's ratio	Density (Kg/m^3)	UCS BH335 (MPa)
siltstone	1.3	24	2.5	5	1.7	0.9	2.3	0.28	2710	25
coal	0.5	20	0.01	5	2.11	1.26	3.13	0.24	1600	16

The gob was represented using the double-yield model because the caved material undergoes substantial irreversible compression as it progressively accommodates the load transferred from the overlying strata. The cap-pressure–volumetric-strain relationship was defined according to Salamon's formulation [42] and calibrated using available laboratory and in-situ information. Based on the geological conditions of the investigated panel, the immediate roof thickness above the 1 m coal seam was taken as 5 m. Accordingly, the modeled gob zone has a total height of 6 m, comprising the extracted coal seam and the immediately caved roof strata. Roof caving was controlled using the critical shear strain criterion. With the revised elastic parameters, the critical shear strain was determined as $\gamma c = 0.0062$. Zones in which the calculated shear strain exceeded this threshold were therefore considered susceptible to roof caving and were incorporated into the progressive development of the gob.

The use of the Mohr–Coulomb formulation for the intact coal and surrounding strata was primarily motivated by the objective of the numerical investigation. The purpose was to compare the relative mechanical response of alternative pillar widths under consistent loading and extraction conditions rather than to reproduce detailed post-peak constitutive behavior of the coal. Furthermore, the coal seam is only approximately 1 m thick, and the dominant ground-control mechanisms in the investigated panel are associated with roof failure, caving, gob compaction, and subsequent stress transfer. Under these conditions, the principal focus is on the redistribution of load and its effect on the roadway–pillar system. The double-yield formulation was therefore used specifically for the collapsed material, where irreversible compaction and subsequent load redistribution are the dominant mechanical processes.

The tensile strength of coal was assigned a value of 0.01 MPa based on reported mechanical properties of the Parvadeh coal seams and parameters adopted in previous numerical studies of comparable underground coal-mining conditions. Although this value is considerably lower than the tensile strength commonly associated with intact rock, it is consistent with the weak tensile resistance of coal and allows tensile yielding to be identified as an indicator of crack initiation within the numerical model. Tensile failure was not considered the principal instability mechanism in the investigated pillar–roadway system.

It is recognized that the Mohr–Coulomb formulation does not explicitly reproduce post-peak strain-softening behavior. Nevertheless, maintaining the same constitutive formulation for all pillar-width cases provides a consistent basis for comparative assessment. More advanced simulations incorporating strain-softening behavior, together with systematic uncertainty or sensitivity analysis of the mechanical parameters, could be considered in future investigations to examine their influence on the predicted stability limits.

3.3. Tunnel Excavation and Support System

The maingate and tailgate roadways were modeled using a sequential excavation and support procedure to reproduce the interaction between the advancing excavation and the installed ground-support system. Each roadway was excavated in 1 m increments, followed immediately by installation of the corresponding support. Steel sets with the mechanical properties given in Table 3 were placed at 1 m intervals, and a 10 cm shotcrete layer was applied in conjunction with the steel support. This staged procedure was adopted to provide a more realistic representation of the progressive development of roadway deformation and the transfer of load between the surrounding rock mass and the support elements.

The access tunnels (X-cuts), which provide access to the longwall face and contribute to the ventilation arrangement, were also included in the excavation sequence. Owing to their relatively small width (approximately 1 m) and the comparatively low stress conditions considered for these openings, no additional support was assigned to the X-cuts in the numerical model.

The response of the support system was evaluated together with the mechanical behavior of the surrounding rock and pillars. In particular, support displacement and load–moment responses were monitored for the different pillar-width configurations, ranging from 4 to 12 m. This enabled the effects of pillar geometry and progressive gob compaction on roadway deformation and support demand to be examined within a common numerical framework.

ACCEPTED MANUSCRIPT

Table 3. Mechanical properties of the steel sets used in the numerical model

Young's modulus (Pa)	Poisson's ratio	Cross-sectional area	Second moment of area about the z-axis (Iz)	Second moment of area about the y-axis (Iy)	Polar moment of inertia (J)
2E+11	0.25	2.01E-3	8.69E-6	8.69E-6	0

The mechanical properties assigned to the shotcrete are presented in Table 4. In the numerical model, the shotcrete properties are defined by its Young's modulus, Poisson's ratio, and cross-sectional area. The corresponding parameters were selected according to the support characteristics used in the mine.

Table 4. Mechanical properties of the shotcrete used in the numerical model

Young's modulus (Pa)	Poisson's ratio	Cross-sectional area
18E+9	0.15	0.1

3.4. Modeling of Access Galleries (X-cuts)

Following the excavation and installation of support in the maingate and tailgate roadways, access galleries (X-cuts) were introduced to establish connections between the longwall face and the main gate entries. To reproduce the sequence adopted in the mining operation, these galleries were excavated incrementally after each 10 m advance of the caving front.

The numerical results showed localized increases in stress around the junctions between the X-cuts and the gate roadways. These concentrations were mainly associated with the change in excavation geometry at the intersections and the discontinuity of the shotcrete lining in these areas. The calculated maximum vertical stress within the access galleries was approximately 2.0–2.5 MPa.

Despite the localized stress concentration at the intersections, the relatively small gallery width (approximately 1 m) and the low overall stress level did not indicate a requirement for additional support. Therefore, no supplementary support elements were assigned to the X-cuts in the numerical simulations. The resulting stress distribution around the access galleries is illustrated in Fig. 4.

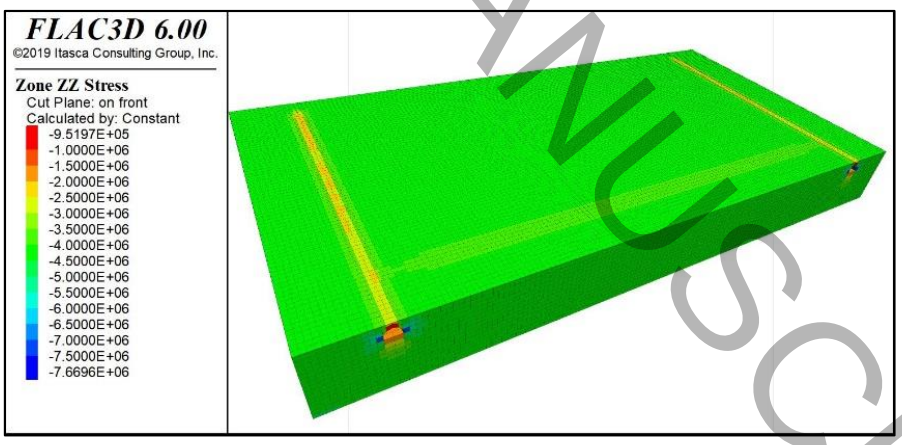

Fig. 4 Stress distribution in the access tunnel

3.5. Simulation of Progressive Longwall Extraction

The advance of the longwall face was reproduced numerically according to the sequence followed in the C1W4 panel. Each mining cycle consisted of a 1 m cutting step, followed by removal of the temporary supports and subsequent roof caving. To represent the progressive nature of the extraction process, five consecutive 10 m face-advance stages were simulated. This procedure allowed the evolution of the stress field and

ACCEPTED MANUSCRIPT

deformation response to be examined as the caved zone developed and the load was progressively transferred toward the surrounding coal pillars and gate roadways. The simulations provided information on abutment and front stresses, roof displacement, and the stress–strain response of the pillars and adjacent strata.

The extraction procedure, roadway-support representation, and gob constitutive model were considered together to characterize the mechanical response of the longwall system. Accordingly, the numerical framework provided the basis for assessing roadway stability, support demand, and changes in pillar behavior associated with progressive gob development. The results obtained from these simulations are subsequently used in the performance assessment and field validation presented in Sections 4 and 5.

Roof collapse was initiated according to the critical shear-strain criterion proposed empirically by Sakurai (Eqs. (1)–(2)). In this approach, caving is assumed to begin when the calculated shear strain in the immediate roof exceeds the corresponding critical value. The elastic parameters required by the Sakurai relationship were obtained from the bulk and shear moduli assigned to the immediate roof material in the FLAC3D model.

$$\log \varepsilon_c = -0.25 LogE - 1.22 \tag{1}$$

$$\gamma_c = (1 + \vartheta) * \varepsilon_c \tag{2}$$

An important consideration in applying Eq. (1) is the unit system of the empirical relationship. The deformation modulus, E, must be introduced in kg/cm² because the original Sakurai formulation was developed using this unit. Therefore, the Young's modulus of the immediate-roof siltstone used in the numerical model, equal to 2300 MPa, was first converted to kg/cm², giving approximately 23,445 kg/cm². Substitution of this value into the empirical relationship resulted in a critical shear strain of $\gamma_c = 0.0062$.

This value was subsequently adopted as the threshold for initiating roof caving in the numerical simulations. Thus, zones in which the computed shear strain exceeded γc were considered to have reached the onset of failure and were converted into gob material.

The critical strain obtained from the Sakurai relationship represents a caving-initiation criterion rather than an intrinsic strength parameter of the rock. Consequently, its value was calculated directly from the empirical formulation using the mechanical properties determined for the immediate roof at Parvadeh IV. Although the criterion provides a practical basis for representing progressive roof collapse, uncertainty associated with the use of an empirical caving threshold remains a limitation of the present modeling approach.

Once the critical shear-strain condition was satisfied, the failed roof zones were represented as caved material. The double-yield constitutive model was employed to simulate the subsequent mechanical response of the gob. Unlike intact rock, the fragmented material within the caved zone undergoes substantial irreversible compression as the overlying strata progressively load the gob. The adopted formulation therefore permits volumetric compaction and the associated redistribution of stress to be incorporated into the analysis.

The cap-pressure–volumetric-strain relationship for the gob was established using the Salamon formulation given in Eq. (3) [5,42]:

$$P_c = \frac{E_0}{1 - \frac{\varepsilon_V}{\varepsilon_V^m}} \tag{3}$$

The initial deformation modulus of the caved material, E0, was determined from empirical relationships developed for gob-compaction behavior. These relationships account for the strength characteristics of the fragmented roof material and the thickness of the extracted seam. In the present study, the parameter b was determined from the coal-seam thickness and the strength classification of the immediate roof, while the coefficients c1 and c2 were selected according to the corresponding roof-strength category.

Based on the laboratory uniaxial compressive strength measurements and the geological characterization of the C1W4 immediate roof, the material was classified as weak rock. Accordingly, the coefficients (c1 = 6.2 and c2 = 32) were adopted. The parameters used to establish the mechanical response of the gob are summarized in Tables 5–8.

The density assigned to the gob was lower than that of intact siltstone to account for the fragmented and

ACCEPTED MANUSCRIPT

loosened condition produced by roof collapse. A density of 1500 kg/m³ was adopted for the caved material. Relative to the intact siltstone density, this corresponds approximately to a reduction factor of 1.8. This factor should be interpreted as an equivalent numerical representation of the increased void space and loosened structure of the caved material within the double-yield formulation, rather than as a direct field measurement of the actual bulking ratio.

The vertical extent of the caving zone was set to 6 m, consisting of the 1 m extracted coal seam together with approximately 5 m of immediate roof strata. The height of the immediate roof participating in caving was estimated using the empirical relationship proposed by Abdellah et al., which relates the caving height to the coal-seam thickness and the strength characteristics of the overlying strata. The resulting estimate was consistent with the geological investigations and field observations at Parvadeh IV, where approximately 5 m of immediate roof was observed to participate in the caving process.

After the failed zones were converted to gob and the corresponding double-yield properties were assigned, the numerical model was solved at each extraction stage. The resulting stress, displacement, plasticity, and stability responses were then obtained for the successive caving stages using Eqs. (4)–(6) [6,15].

$$E_0 = 10.39\frac{\sigma_c^{1.042}}{b^{7.7}} \tag{4}$$

$$b = \frac{c_1 h + c_2}{100} + 1 \tag{5}$$

$$H_c = \frac{100h}{c_1 h + c_2} \tag{6}$$

Table 5. Strength coefficients for roof strata

Roof rock strata	Strength	Coefficient C1	Coefficient C2
Strong	> 40 MPa	2.1	16
Moderate	20–40 MPa	4.7	19
Weak	< 20 MPa	6.2	32

Table 6. Properties of the roof strata

b	h	C1	C2	σ_c	E0
1.4	1	6.2	32	3	2.45

Table 7. Cap-pressure versus volumetric-strain values

Pc	0	0.5	1.0	1.5	2.0	2.5	3.0
ε_V	0	0.01	0.021	0.031	0.04	0.048	0.056

Table 8. Mechanical properties of the rocks in the caved zone

Cohesion (MPa)	Tensile strength (MPa)	Density (kg/m^3)	Bulk Modulus-Maximum (MPa)	Shear-Maximum (MPa)
0.01	0	1500	13.88	150

This staged solution procedure enabled the progressive interaction between face advance, roof failure, gob compaction, stress transfer, and pillar response to be tracked throughout the simulated extraction sequence. The resulting numerical outputs form the basis for the comparative evaluation of the five pillar-width configurations presented in the following sections.

ACCEPTED MANUSCRIPT

ACCEPTED MANUSCRIPT

4. Results and Analysis

The FLAC3D simulations were used to characterize the evolution of the stress field, ground deformation, and support response associated with progressive longwall extraction in the C1W4 panel. The analysis focused primarily on the behavior of the maingate roadway and the response of the panel pillars under the five investigated pillar-width configurations. Particular attention was given to the manner in which face advance and gob development modify the distribution of vertical stress around the excavation and pillar system.

4.1. Abutment Stress and Global Stress Redistribution

The stress distributions obtained at the final simulated extraction stage reveal the characteristic redistribution of load produced by longwall mining. Following face advance and roof caving, the extracted region experiences substantial stress relief, whereas the load released from the excavated zone is transferred toward the surrounding coal pillars and the advancing face. Consequently, pronounced stress concentrations develop above the pillars, followed by a gradual return toward the initial stress state with increasing distance from the mined area.

At the central section of the panel (y = 38 m), the initial vertical stress was approximately 4.0–4.4 MPa. The stress above the tunnel roof increased to approximately 6.3 MPa, corresponding to about 1.5 times the initial in-situ stress. A substantially higher concentration developed above the panel pillars, where peak stresses reached approximately 12.5–14 MPa, equivalent to roughly 3–3.5 times the initial stress. Nevertheless, for pillar widths of 8 m and greater, the calculated stress concentrations remained below the estimated peak strength of the corresponding pillars. Within the central portion of the gob, the vertical stress decreased by approximately 66%, demonstrating the transfer of a considerable portion of the released load toward the surrounding load-bearing zones (Fig. 5).

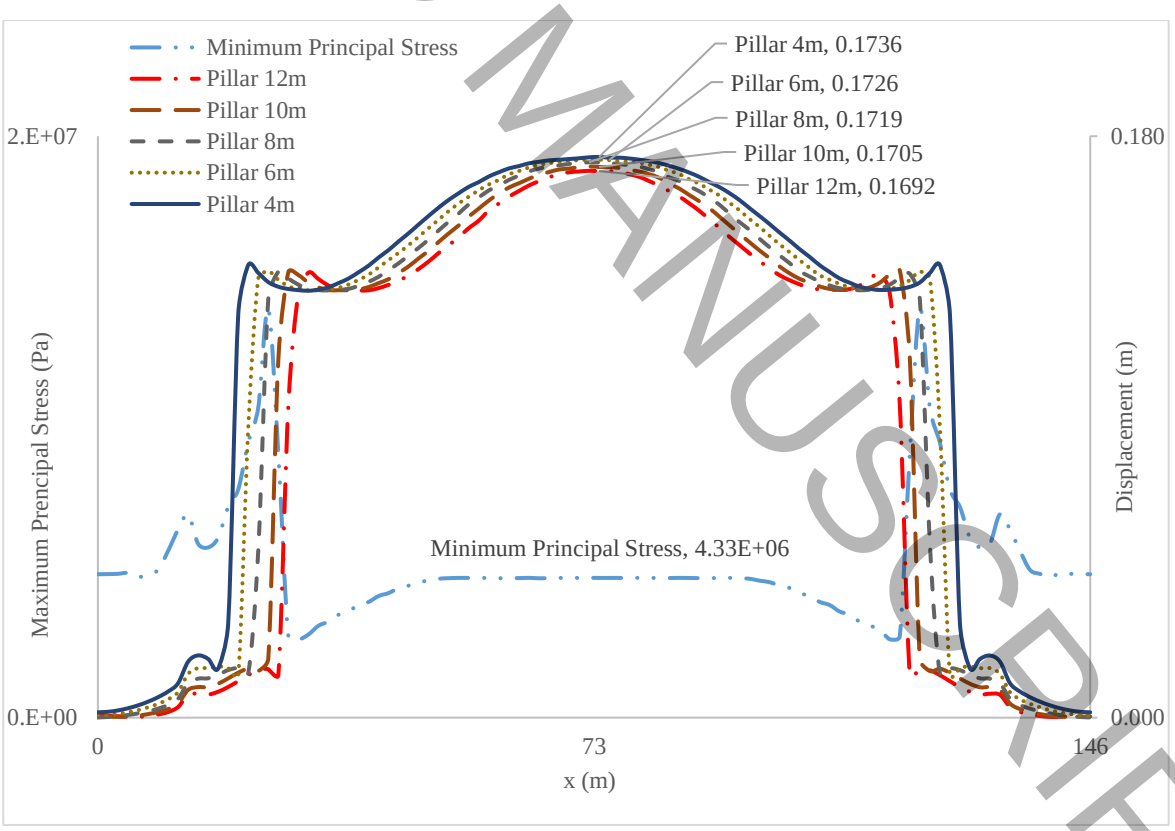

Fig. 5 Stress and displacement profiles at the middle section of the extracted zone after the fifth mining step

A separate assessment was performed along the unmined coal ahead of the advancing face at y = 68 m. The resulting profiles show the development of a front abutment-stress concentration immediately ahead of the face. The maximum front abutment stress occurred approximately 2–3 m in front of the longwall face, with the peak value at the face center reaching about 10.4 MPa. This value corresponds to approximately 2.6 times the initial in-situ stress. The stress above the main tunnel roof was approximately 5.46 MPa, or about 1.4 times the initial stress, whereas the stress above the pillar decreased to approximately 4.7–4.72 MPa as a result of the local redistribution of the stress field (Fig. 6).

The maximum-principal-stress profiles in Fig. 6 further illustrate the spatial development of this front abutment zone. The stress concentration is most evident near the center of the advancing face and around the roofs of the main entries. Moving away from these regions, the stress progressively decreases and subsequently approaches the overburden stress toward the pillar zone and the outer model boundaries. The relatively low stress levels calculated within the panel pillars and in the immediate vicinity of the tunnels reflect the local stress-relief effects associated with excavation. The location and intensity of these concentrations vary slightly among the five pillar-width configurations, although the change in peak stress magnitude is comparatively limited.

The corresponding roof-displacement profiles are also presented in Fig. 6. At the center of the longwall face, the calculated roof displacement varied from approximately 4 to 6 mm among the investigated pillar widths. Above the face, the roof displacement was approximately 1 cm. These results indicate that changes in pillar width influence the deformation response and the spatial distribution of stress more noticeably than they alter the overall magnitude of the principal stress concentration.

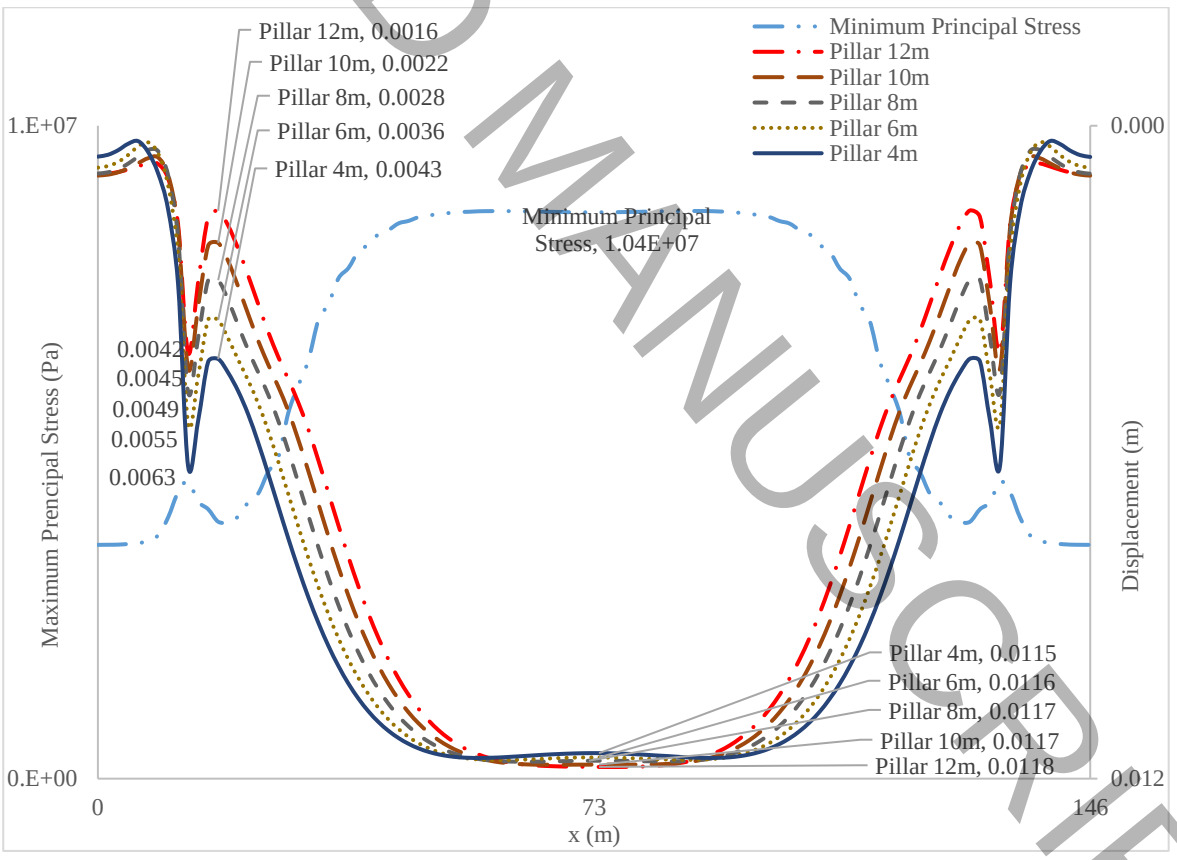

Fig. 6 Stress and displacement profiles at the middle section of the extracted zone after the fifth mining step

ACCEPTED MANUSCRIPT

The vertical-stress contours for the five pillar-width configurations are shown in Fig. 7. The overall pattern confirms that the largest vertical stresses develop in the vicinity of the active longwall face and, particularly, above the panel pillars. Increasing or decreasing the pillar width produces only a relatively small change in the maximum stress magnitude; however, the position of the high-stress zone changes according to the pillar geometry. This behavior indicates that pillar width has a stronger effect on the spatial concentration and localization of mining-induced stress than on the global magnitude of the vertical stress field.

The minimum vertical stress, approximately 0.7 MPa, was obtained near the corners of the extracted region, where the influence of excavation produced pronounced stress relief. In contrast, the vertical stress acting above the panel pillars reached approximately 14 MPa, equivalent to about 3.5 times the initial in-situ stress. At locations sufficiently far from the extraction zone, the calculated vertical stress remained close to the applied overburden stress, indicating that the influence of longwall excavation diminished rapidly toward the model boundaries.

Around the gate-roadway section, the vertical stress above the tunnel roof generally ranged from approximately 1 to 2 MPa. In the tunnel section located ahead of the advancing face, the stress progressively recovered toward the initial in-situ level. Along the sidewall facing the longwall panel, vertical stress values of approximately 3–5 MPa were obtained. The local variation in this region was mainly associated with the presence and excavation of the access tunnels connecting the gate entries to the longwall face.

(A)

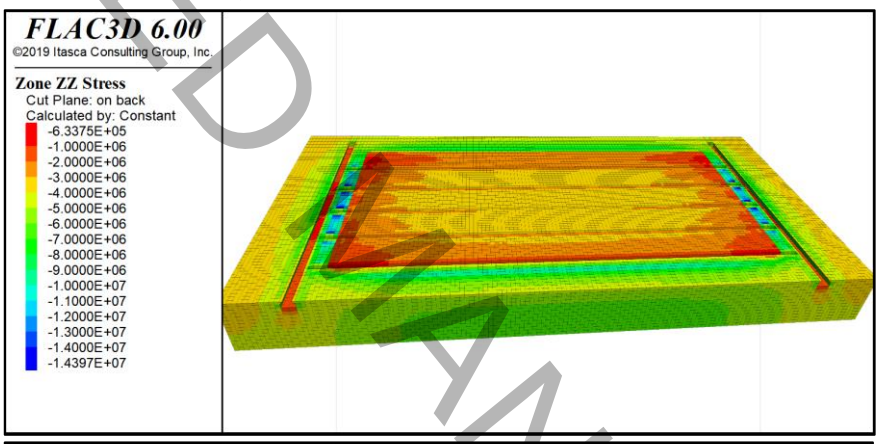

(B)

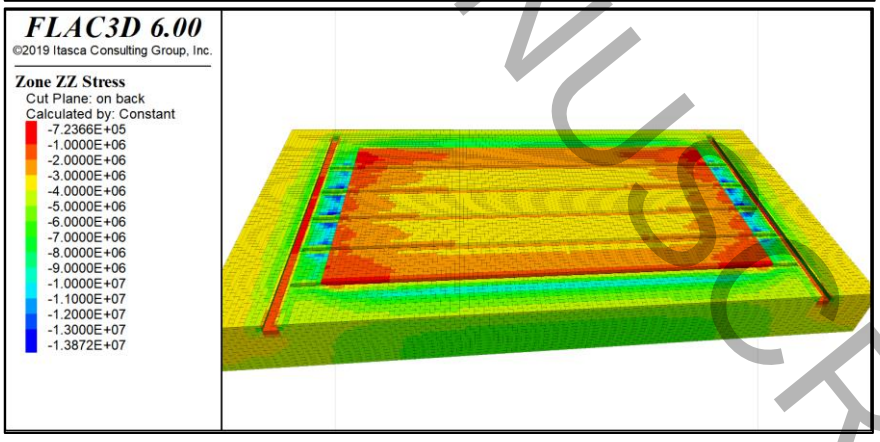

ACCEPTED MANUSCRIPT

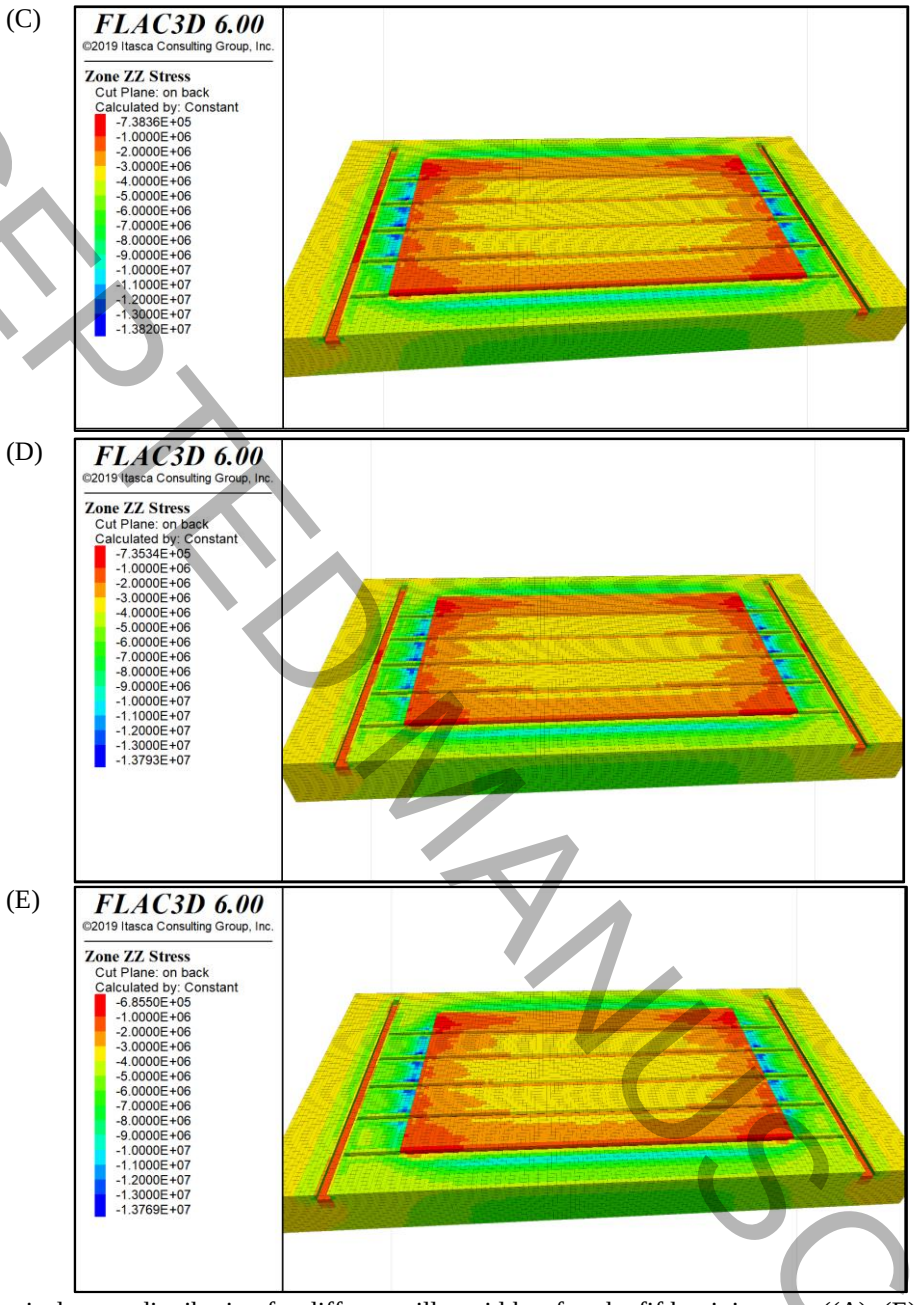

Fig. 7 Vertical stress distribution for different pillar widths after the fifth mining step ((A)–(E): 4, 6, 8, 10, and 12 m pillars)

Overall, the calculated stress contours demonstrate that longwall extraction produces a characteristic combination of stress relief within the excavated zone and load concentration in the surrounding pillars and face-abutment region. The results also emphasize the need to represent both the mechanical response of the surrounding rock mass and the compaction behavior of the gob when evaluating the stability of gate roadways and panel pillars. Because the investigated seam has a very small dip and was treated as essentially horizontal

ACCEPTED MANUSCRIPT

in the numerical model, the front abutment-stress response ahead of and behind the advancing face remained nearly symmetric.

4.2. Displacement Analysis

The deformation response of the modeled excavation system was examined at six representative locations covering the principal components of the roadway–pillar–gob system. These monitoring sections included the two tunnel sidewalls, the tunnel roof, the pillar centerline, the pillar–gob interface, and the central region of the gob. Comparison of the resulting displacement fields shows a consistent reduction in deformation as pillar width increases.

The maximum displacement values obtained at the final simulated extraction stage are summarized in Table 9. The results demonstrate that both roadway-roof movement and deformation above the pillar centerline decrease progressively with increasing pillar width.

Table 9. Maximum displacement values for different pillar widths at the fifth mining step

Pillar width (m)	Tunnel roof displacement (mm)	Displacement above pillar centerline (mm)
4	17	24.3
6	13	20.7
8	10.7	17.7
10	8.6	15.2
12	7.2	13.0

At the investigated extraction stage, the maximum deformation within the gob reached approximately 30 cm. Such a large displacement is consistent with the expected compaction and closure associated with roof caving and the progressive development of the collapsed zone (Fig. 8). In contrast, the displacements calculated around the gate roadways remained within the acceptable range for all five pillar configurations. Nevertheless, the substantially larger deformation obtained for pillars narrower than 8 m indicates a progressive deterioration in pillar behavior as the available load-bearing width decreases.

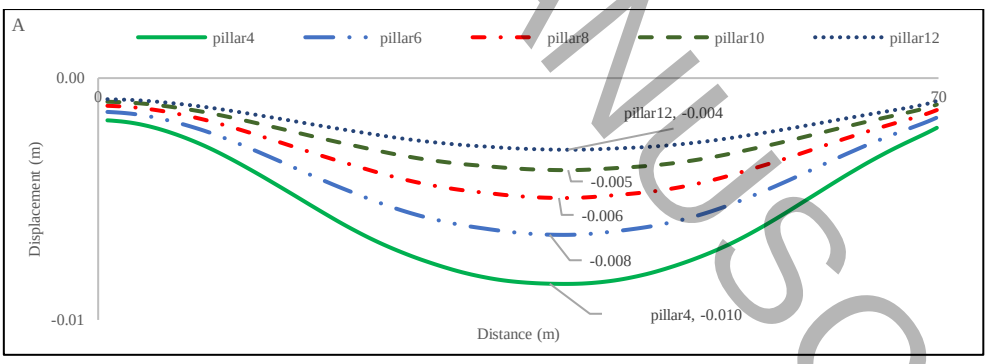

ACCEPTED MANUSCRIPT

Three-Dimensional Numerical Investigation of Ground Response and Stability of Gate Roadways and Pillars in Longwall Mining

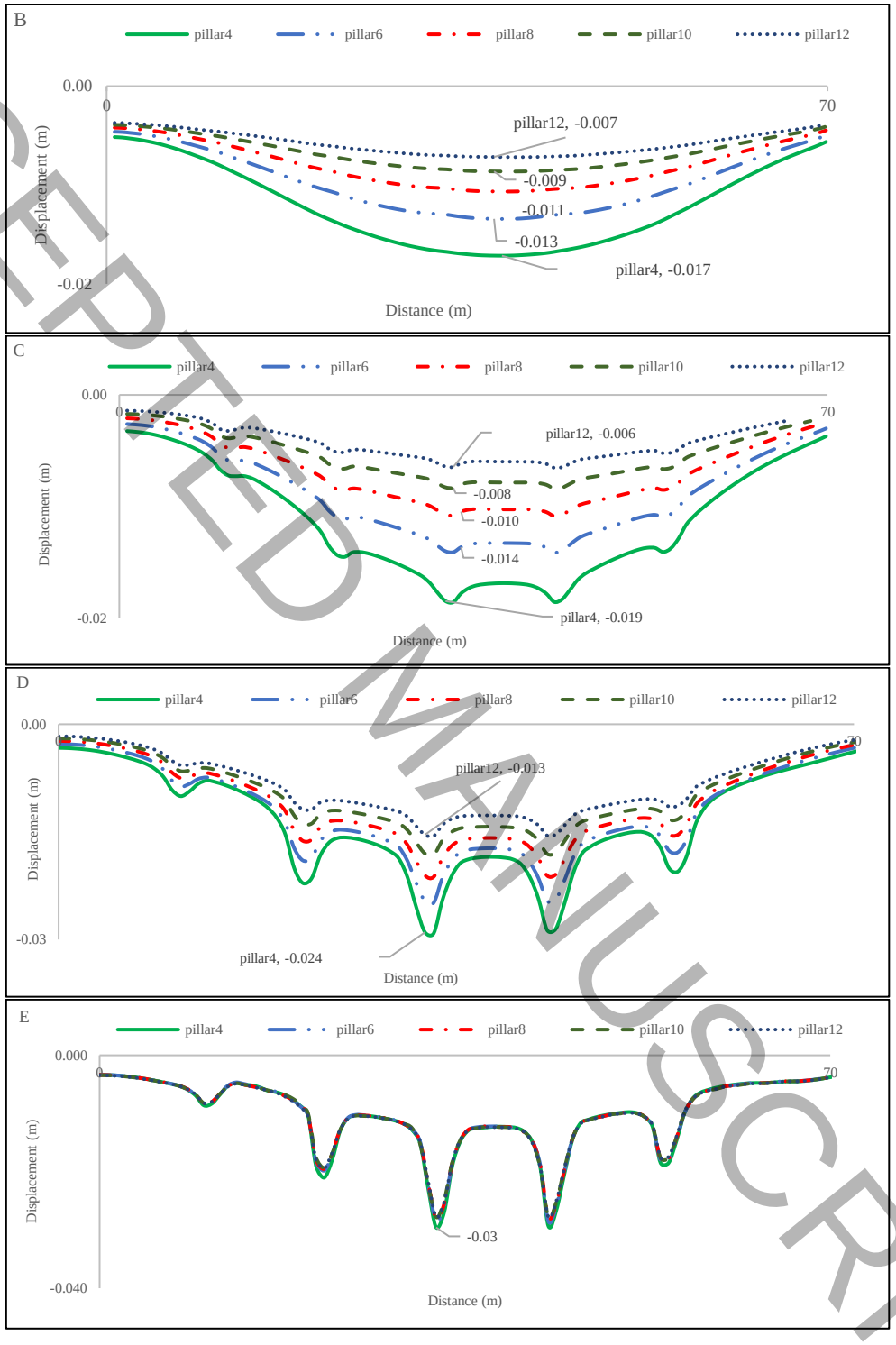

ACCEPTED MANUSCRIPT

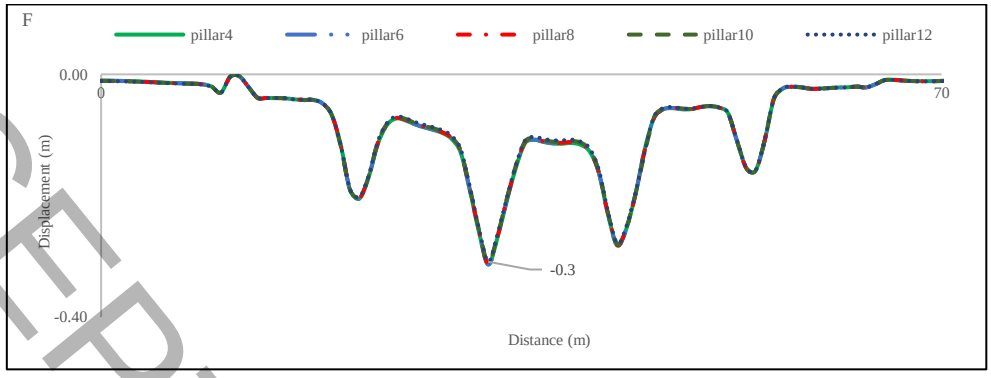

Fig. 8 Displacement profiles at different monitoring sections for the investigated pillar widths after the fifth mining step ((A)–(F): tunnel wall on the intact-coal side, tunnel roof, tunnel wall on the gob side, center of the pillar between the tunnel and gob, pillar–gob interface, and center of the gob)

The evolution of tunnel-roof deformation during face advance is presented in Fig. 9. For all configurations, roof displacement increased as the extraction front progressed. The position of the maximum deformation also gradually shifted toward the central portion of the gob, reflecting the progressive influence of excavation and caving on the surrounding strata. The magnitude of this response was strongly dependent on pillar width.

Over the five simulated caving stages, the peak tunnel-roof displacement increased from approximately 7 to 17 mm for the 4 m pillar. The corresponding ranges were approximately 6.4–13.4 mm for the 6 m pillar, 6.0–10.7 mm for the 8 m pillar, 5.7–8.6 mm for the 10 m pillar, and 5.4–7.2 mm for the 12 m pillar. Thus, although all configurations exhibit increasing deformation with face advance, wider pillars substantially restrict the magnitude of roof movement.

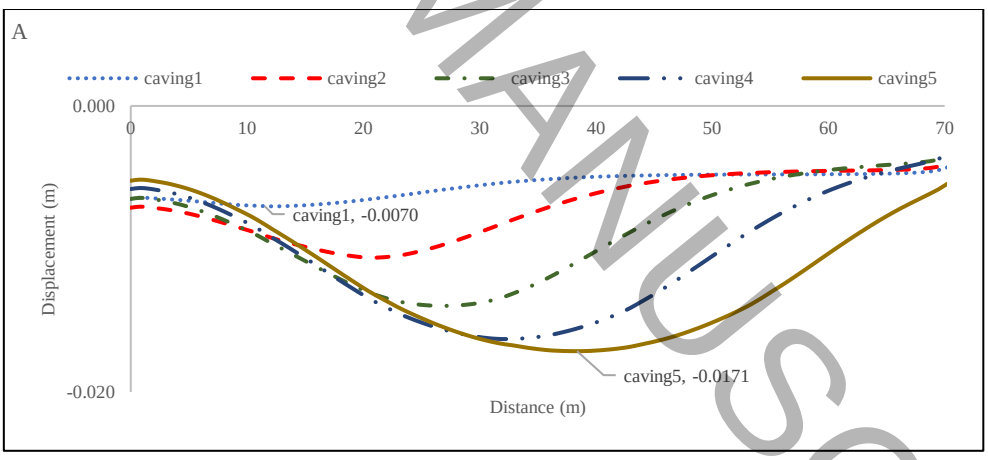

ACCEPTED MANUSCRIPT

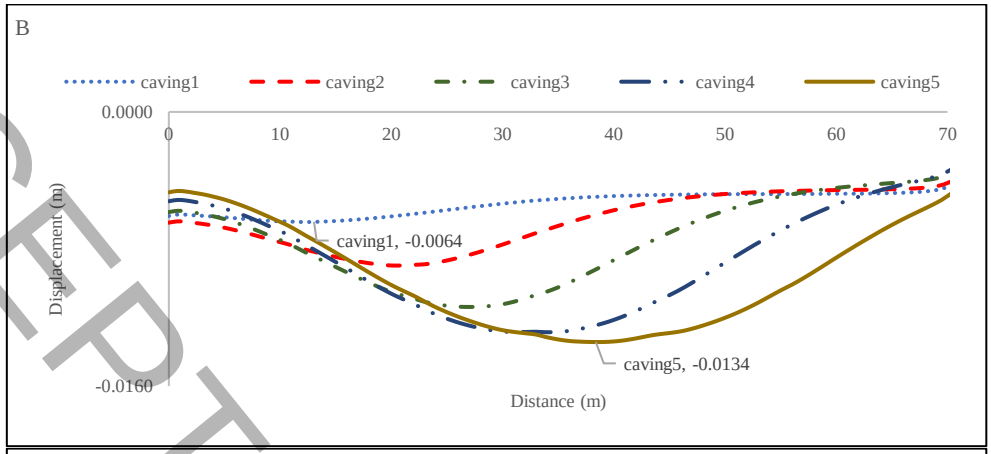

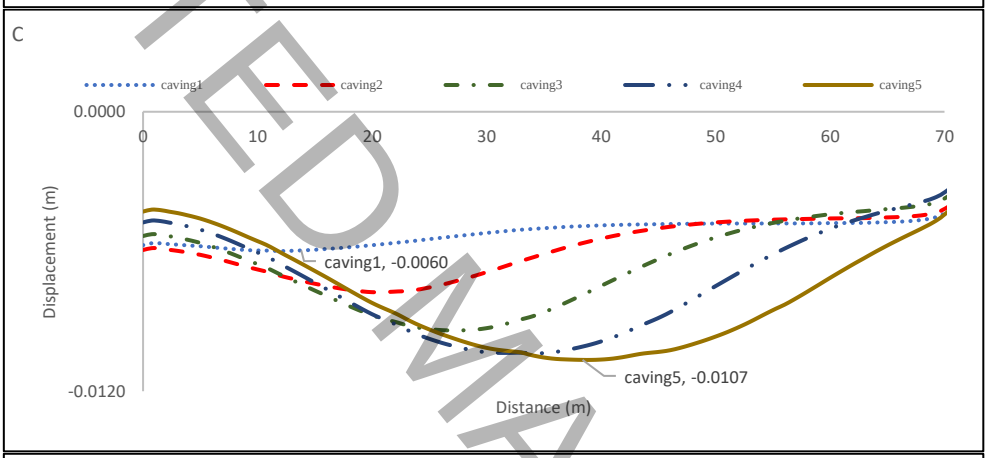

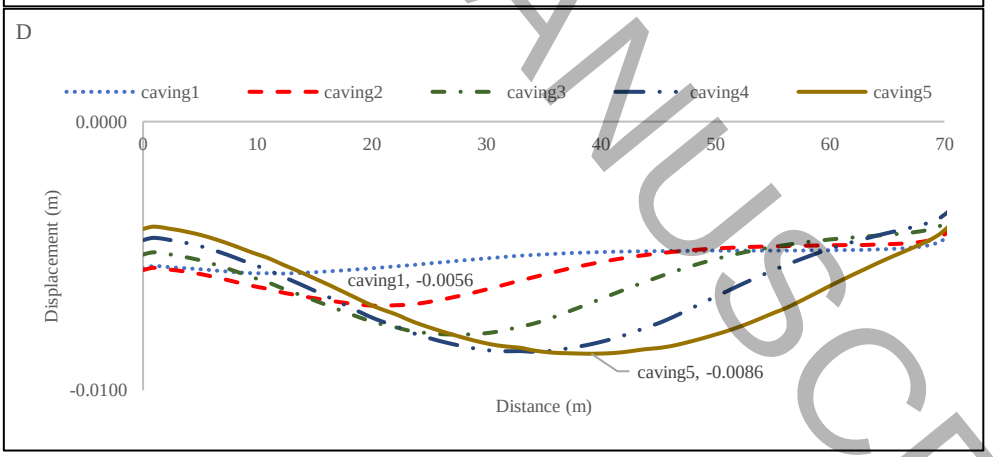

ACCEPTED MANUSCRIPT

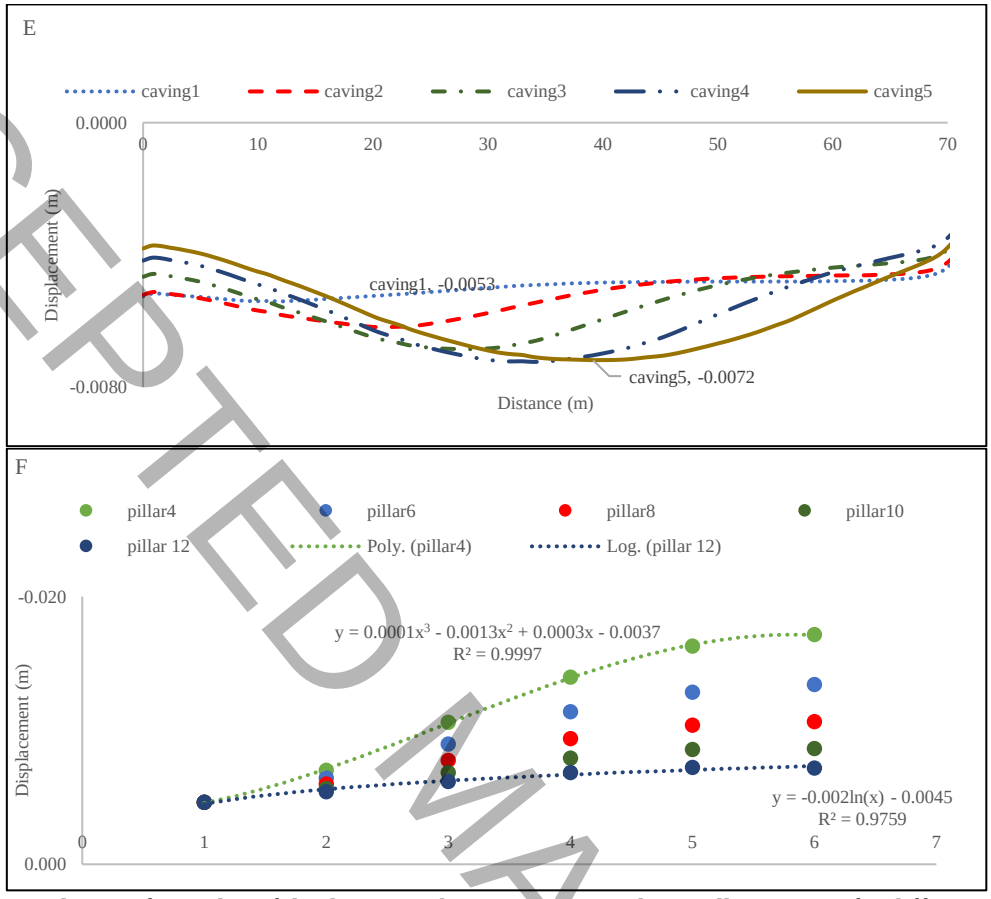

Fig. 9 Evolution of tunnel-roof displacement during progressive longwall extraction for different pillar widths ((A)–(E): displacement profiles for 4, 6, 8, 10, and 12 m pillars at the five mining stages; (F): variation in maximum and minimum displacement values)

A similar but more pronounced trend is observed for deformation above the pillar centerline (Fig. 10). As the longwall face advances, displacement progressively increases and the zone of maximum movement tends to migrate toward the gob center. The 4 m pillar exhibits the largest deformation response, with peak values increasing from approximately 5.5 mm at the initial simulated stage to 24.3 mm at the fifth stage. For the 6 m pillar, the corresponding range is approximately 4.7–20.7 mm, while the 8 m pillar shows values between about 4.1 and 17.7 mm.

For the wider configurations, the maximum displacement is further reduced. The calculated range is approximately 3.7–15.2 mm for the 10 m pillar and 3.4–13.0 mm for the 12 m pillar. The progressive reduction in deformation with increasing pillar width indicates that a larger load-bearing coal section provides greater resistance to mining-induced ground movement and limits the transmission of deformation toward the roadway.

ACCEPTED MANUSCRIPT

Three-Dimensional Numerical Investigation of Ground Response and Stability of Gate Roadways and Pillars in Longwall Mining

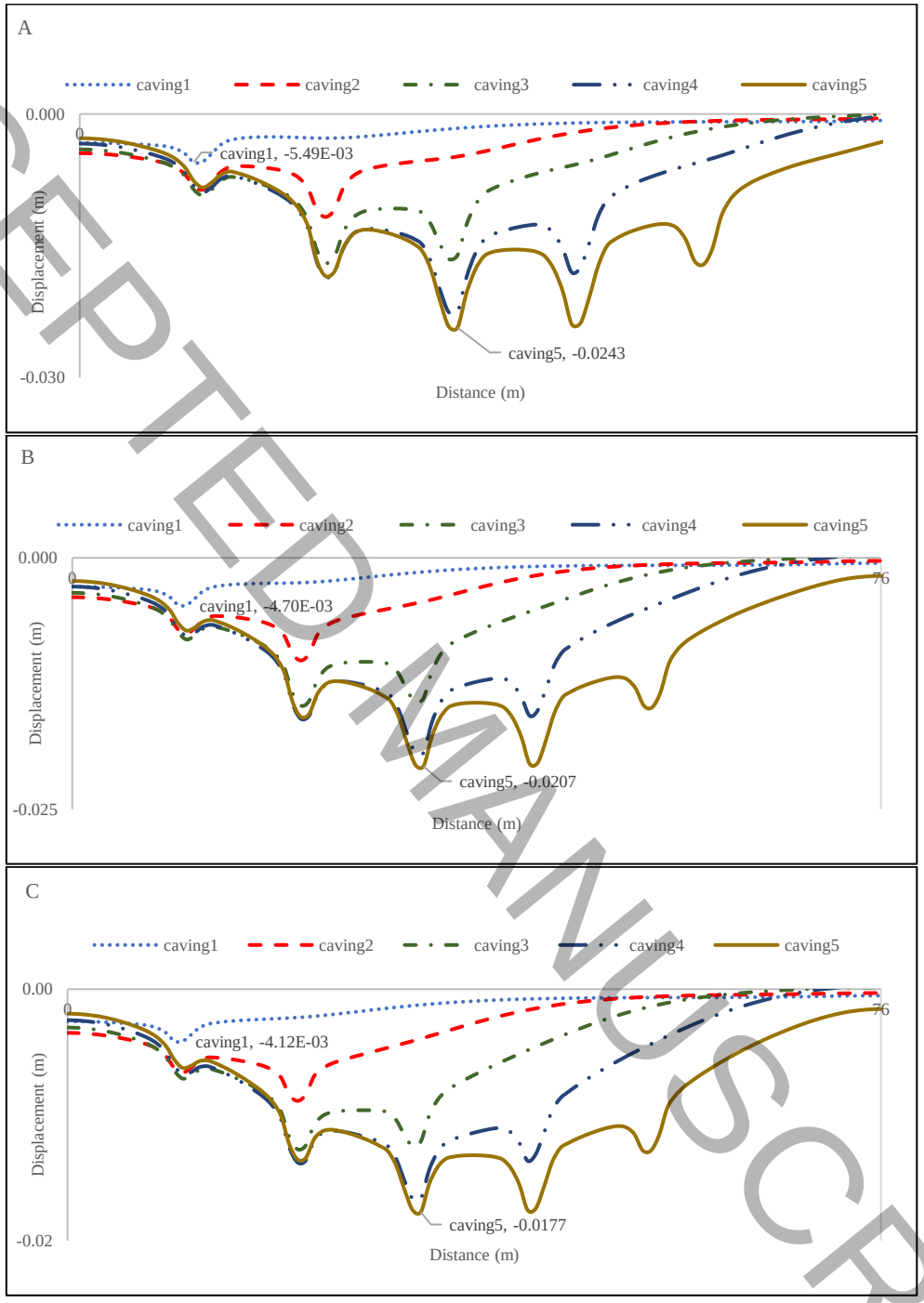

ACCEPTED MANUSCRIPT

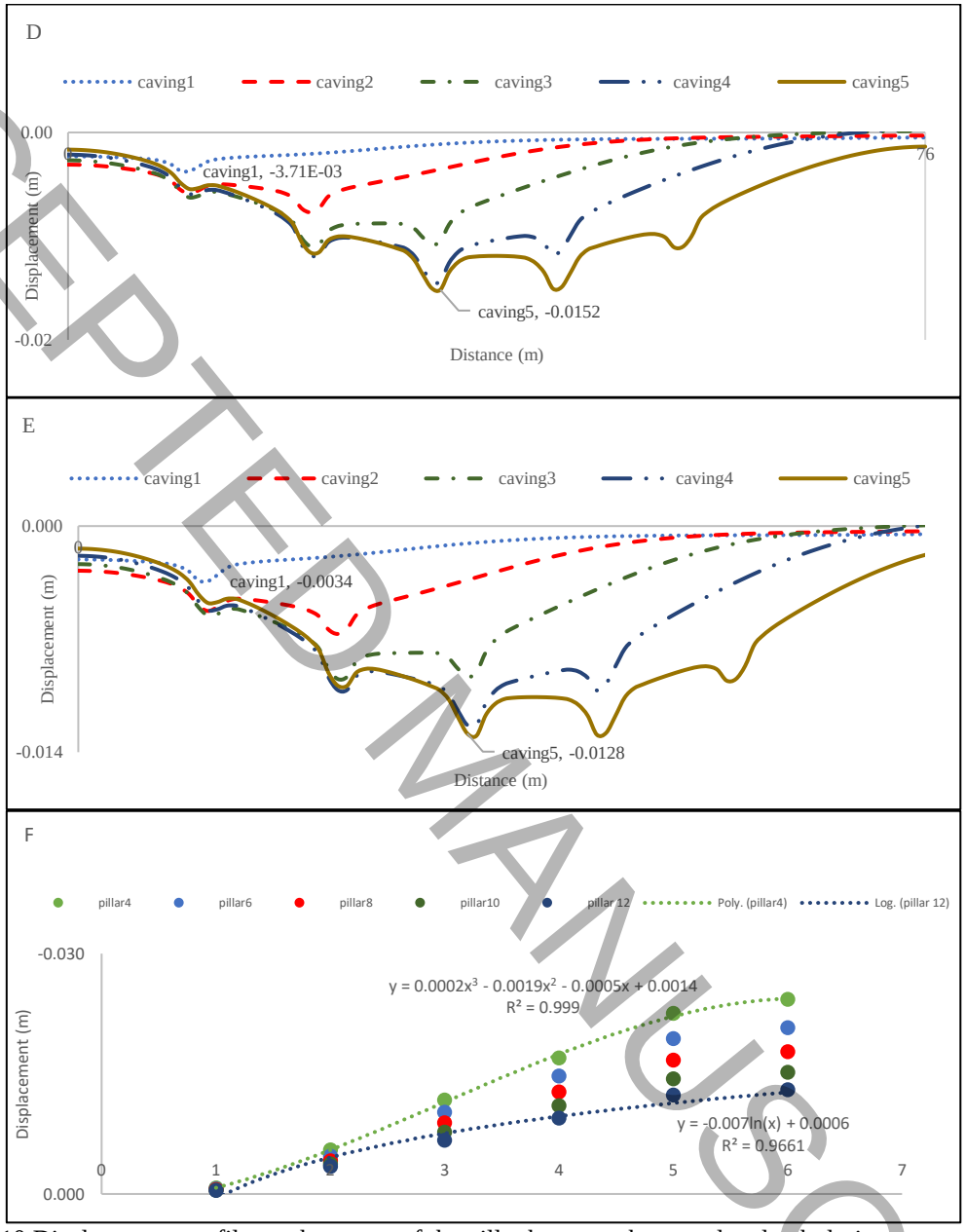

Fig. 10 Displacement profiles at the center of the pillar between the tunnel and gob during progressive longwall extraction for different pillar widths ((A)–(E): pillar widths of 4, 6, 8, 10, and 12 m; (F): variation trend of maximum and minimum displacement)

4.3. Critical Shear Strain Assessment

The Sakurai empirical criterion was used to quantify the shear-strain level associated with the initiation of significant roof deformation and caving. For the immediate roof of the C1W4 panel, the resulting critical shear strain was determined as

ACCEPTED MANUSCRIPT

ACCEPTED MANUSCRIPT

γc=0.0062

The calculated shear-strain distributions indicate that the deformation levels around the tunnel roof and sidewalls remained below this threshold for all five pillar-width configurations. Higher shear strains were instead concentrated near the pillar–gob boundary and within the caved region, where progressive extraction induces substantial stress redistribution and load transfer. The magnitude of these localized strains was generally greater for the narrower pillars.

The most notable response occurred at the centerline of the 4 m pillar, where the maximum shear strain reached approximately 0.008–0.010 and consequently exceeded the adopted critical value of 0.0062. The corresponding maximum value for the 6 m pillar was approximately 0.0042, remaining below the threshold. The 8 m configuration exhibited a still lower maximum value of approximately 0.0034, while the 10 and 12 m pillars showed comparatively smaller and more controlled shear-strain responses.

Accordingly, the Sakurai criterion identifies the 4 m configuration as the only case in which the critical shear-strain threshold is exceeded at the pillar centerline. The centerline response of the 6–12 m pillars remains below the adopted limit. This criterion was, however, treated as one component of the overall stability assessment. The final interpretation of pillar performance also incorporated SSR, plastic-zone development, displacement, and support-system behavior, since exceedance of the critical shear strain at a localized region does not by itself define the global stability condition of the pillar.

Figure 11 compares the spatial distribution of maximum shear strain at six representative sections during the fifth mining stage. The selected locations comprise the tunnel sidewall at X = 12 m, tunnel roof at X = 13.5 m, tunnel sidewall adjacent to the pillar at X = 15 m, the pillar centerline, the pillar edge at the gob interface, and the center of the longwall face. At Section 1, the maximum shear strain varied from approximately 0.0013 to 0.0031. The corresponding ranges were about 0.0035–0.0040 at Section 2 and 0.0014–0.0023 at Section 3. At the pillar centerline (Section 4), the values ranged from approximately 0.0024 to 0.0086, showing the strongest dependence on pillar width among the principal load-bearing sections.

Higher strain levels were obtained at the pillar–gob interface (Section 5), where maximum values ranged from approximately 0.0112 to 0.0127. Similarly, the central region of the longwall face (Section 6) exhibited values between approximately 0.0015 and 0.0136. The relatively high strain recorded at the pillar–gob boundary is associated with the localized interaction between the yielding outer portion of the pillar and the progressively compacting gob. Therefore, exceedance of γc at this interface should not be interpreted in the same manner as exceedance at the intact pillar core. For this reason, the centerline response was given greater weight when assessing the condition of the load-bearing portion of the pillar.

Across the six monitored sections, a general increase in maximum shear strain was observed as pillar width decreased. The 4 m configuration consistently produced the largest or among the largest strain concentrations, confirming its greater susceptibility to localized yielding and deformation under the investigated extraction conditions.

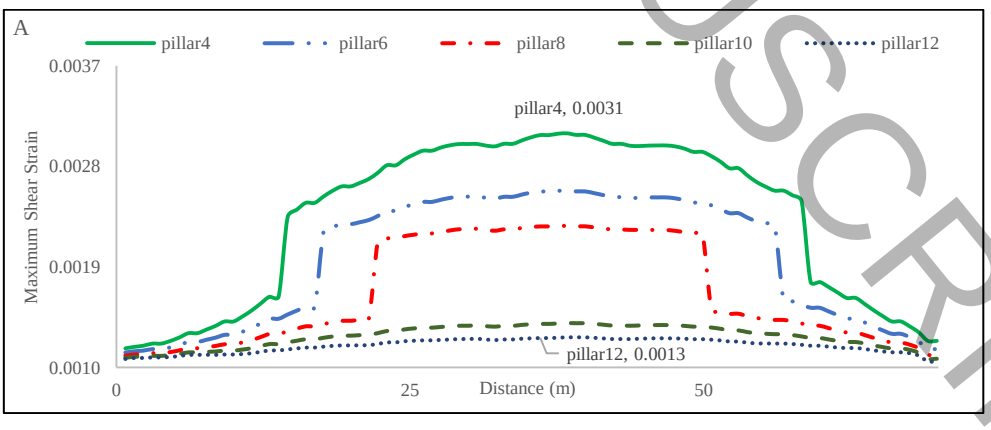

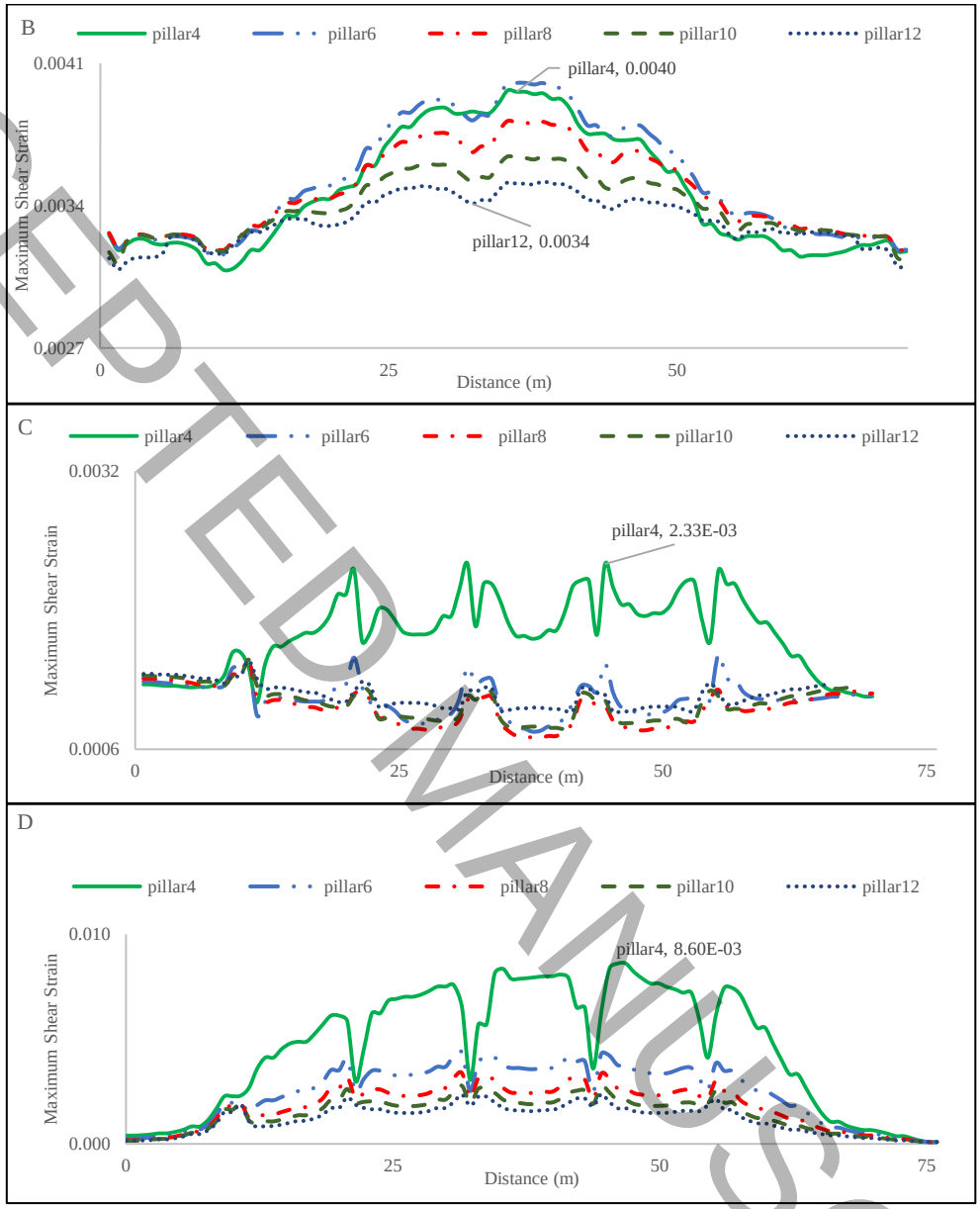

ACCEPTED MANUSCRIPT

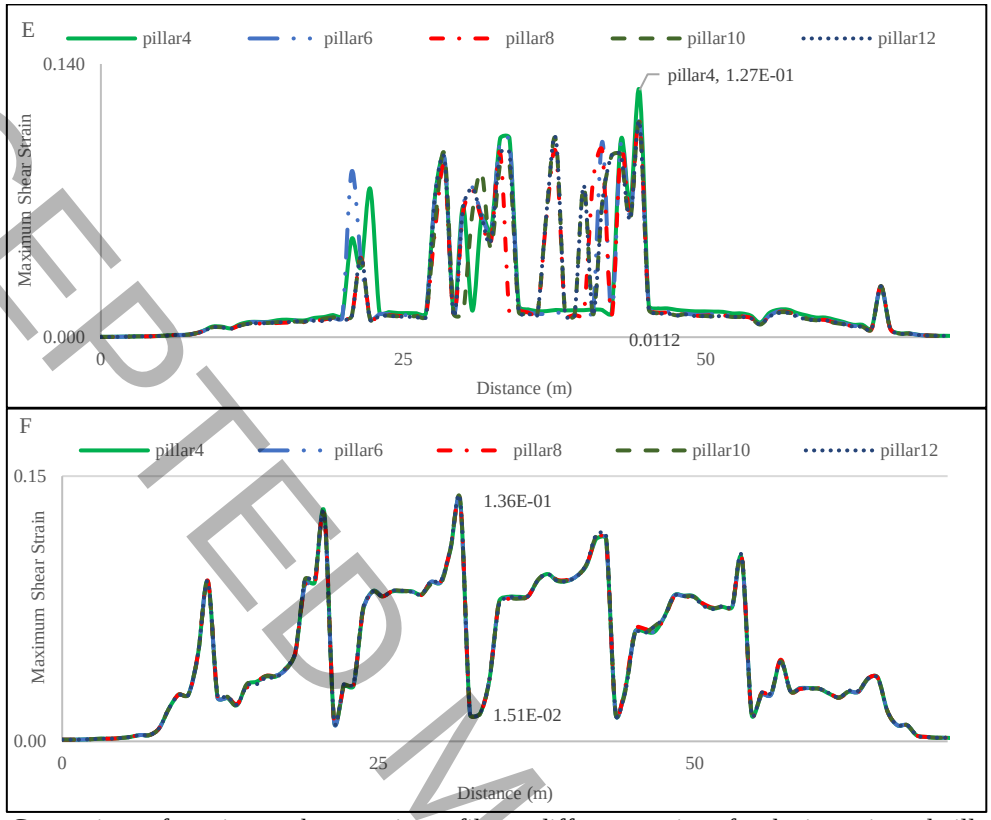

Fig. 11 Comparison of maximum shear-strain profiles at different sections for the investigated pillar-width configurations ((A) tunnel wall on the intact-coal side; (B) tunnel roof; (C) tunnel wall on the gob side; (D) center of the pillar between the tunnel and gob; (E) pillar–gob interface; (F) center of the longwall face)

While Fig. 11 describes the spatial distribution of shear strain at the final simulated stage, Fig. 12 tracks its development at the pillar centerline throughout the extraction sequence. The results show that shear strain generally increases as the face advances, reflecting the progressive transfer of load from the extracted region toward the remaining coal.

The 4 m pillar undergoes the most pronounced increase and reaches a maximum shear strain of approximately 0.0086 at the fifth caving stage, exceeding $\gamma c = 0.0062$. For the 6 m configuration, the maximum centerline strain increases with extraction but remains below the threshold, reaching approximately 0.0042 at the final stage. The corresponding maximum for the 8 m pillar is approximately 0.0034. The 10 and 12 m configurations maintain comparatively low shear-strain levels throughout the simulated extraction sequence, with their centerline values remaining below the critical threshold.

The progressive evolution shown in Fig. 12 therefore confirms that increasing pillar width reduces the accumulation of shear deformation within the pillar core. At the same time, localized exceedance of the critical strain at the pillar–gob interface is observed for several configurations. Because this region represents the transition between the yielding pillar edge and the compacting gob, its response was considered primarily as evidence of localized interaction rather than as a standalone measure of overall pillar failure. The final stability classification was consequently based on the combined interpretation of shear strain, SSR, plastic-zone development, displacement, and support response.

ACCEPTED MANUSCRIPT

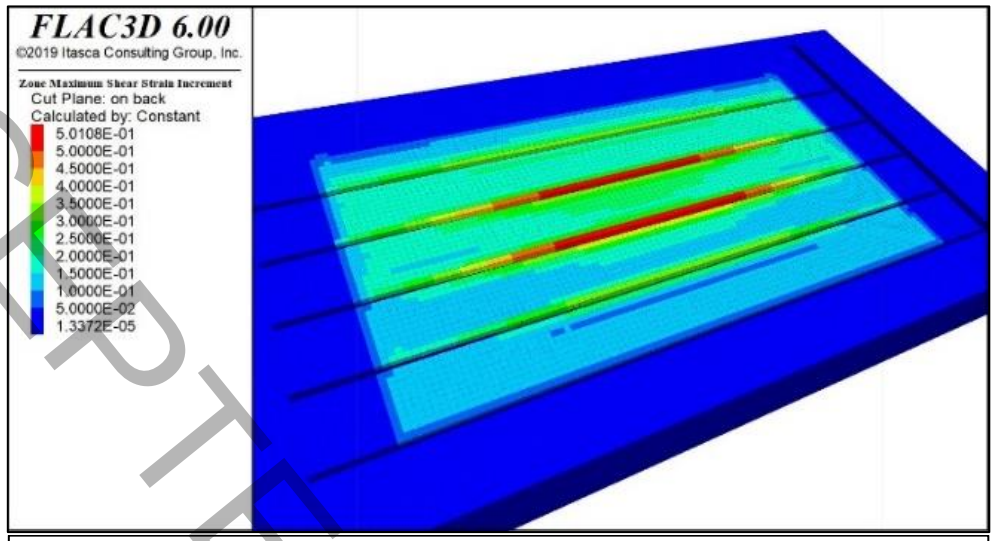

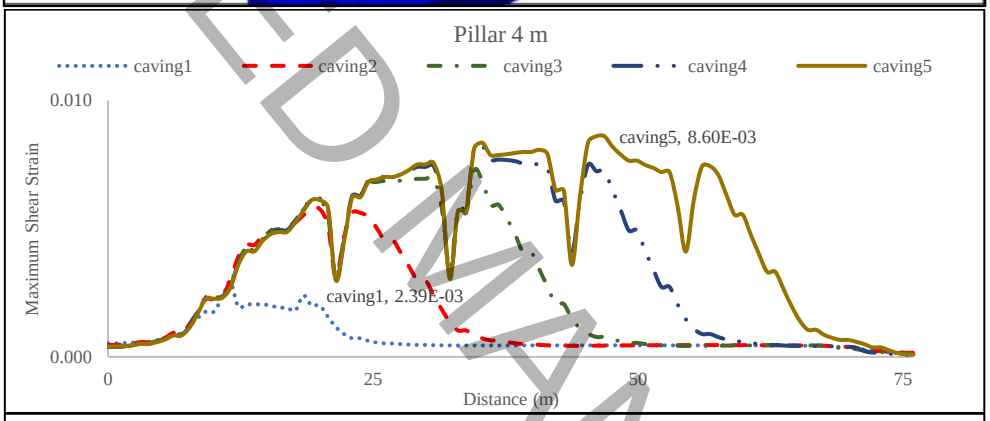

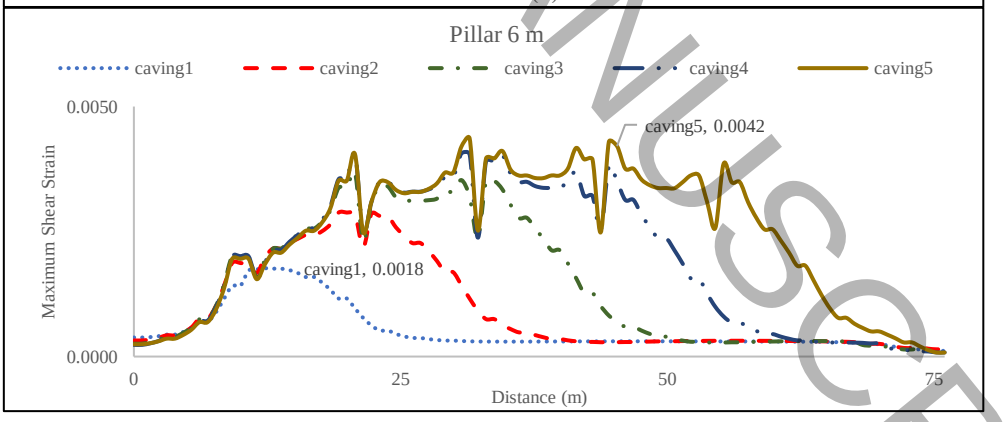

ACCEPTED MANUSCRIPT

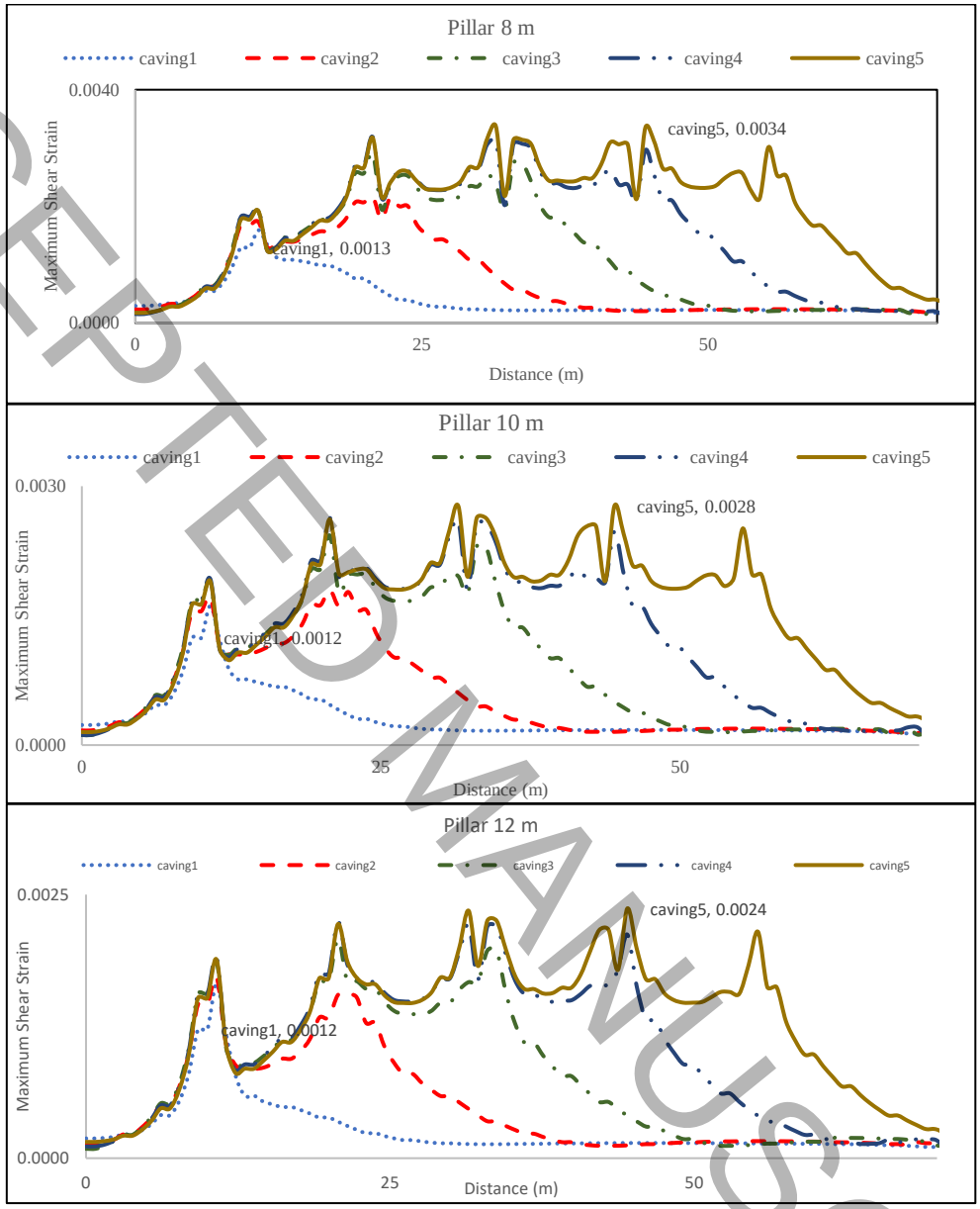

Fig. 12 Evolution of maximum shear strain at the pillar centerline between the tunnel and gob during five successive caving stages for different pillar-width configurations

4.4. Stress–Strength Ratio (SSR) Analysis

The stress–strength ratio (SSR) obtained from the FLAC3D simulations was used as a quantitative measure for assessing the mechanical condition of the gate roadways and panel pillars. This parameter provides a factor-of-safety-type indication by relating the strength available in the modeled material to the stress state generated by excavation and progressive longwall extraction. Within the Mohr–Coulomb formulation, the available strength is determined from the assigned constitutive parameters, including cohesion, friction angle, and tensile strength, while the corresponding stress state is calculated from the mining-induced stress field.

ACCEPTED MANUSCRIPT

An SSR value of 1.4 was adopted as the reference criterion in the present study. This threshold is consistent with the value used by Darvishi et al. [26] for assessing temporary gateroad intersections subjected to longwall-induced loading. Because the maingate and tailgate openings considered here are likewise temporary underground excavations exposed to progressively changing loads during longwall advance, an SSR of 1.4 or higher was considered indicative of an acceptable stability condition, whereas lower values indicate increasing proximity to failure. The adopted threshold should be regarded as an engineering assessment criterion rather than an absolute boundary separating failure from non-failure, since its practical interpretation depends on excavation geometry, loading conditions, support characteristics, and operational requirements.

4.4.1 Tunnel Stability

The calculated SSR distributions show that the gate roadways remain well above the adopted stability criterion. The minimum SSR around the maingate and tailgate tunnels was approximately 4, substantially higher than the reference value of 1.4. This result indicates a considerable strength margin around the modeled roadway sections.

The SSR contours in Fig. 13 further show that the regions surrounding the tunnels maintain comparatively favourable stability conditions for all investigated pillar widths. Although localized variations occur near excavation boundaries and intersections, no extensive low-SSR zones develop around the principal roadway openings. The numerical result is also consistent with the field condition of the C1W4 panel: at the investigated extraction stage, corresponding to approximately 40% of the panel having been extracted, no reported roof or sidewall instability was observed in the maingate or tailgate.

4.4.2 Pillar Stability

In contrast to the relatively high SSR values around the gate roadways, the panel pillars exhibit a pronounced dependence on pillar width. The contour maps in Fig. 13 indicate that reducing pillar width increases the extent of regions with low SSR and promotes a greater degree of yielding within the modeled pillar zone. The 4 and 6 m configurations develop the most extensive low-SSR regions, indicating unfavourable stability conditions under the investigated extraction sequence.

The spatial distribution of SSR at the fifth mining stage is presented in greater detail in Fig. 14. Six representative sections were considered: X = 12 m at the tunnel sidewall, X = 13.5 m at the tunnel roof, X = 15 m at the tunnel sidewall adjacent to the pillar, the pillar centerline, the pillar edge at the gob interface, and the center of the longwall face.

At Section 1, the lowest SSR values were generally associated with the 4 m pillar configuration. Nevertheless, the SSR response varies locally between the excavation boundary and the interior of the pillar. In particular, while portions of the pillar remain above the adopted criterion, the centerline of the narrower pillar configurations can fall below SSR = 1.4 as caving progresses.

At Section 2, localized reductions in SSR occur around the tunnel roof. However, these reductions do not indicate overall roadway instability because the calculated minimum SSR around the principal tunnel sections remains substantially above the adopted criterion. This interpretation is also supported by the absence of reported roadway instability in the field. Section 3 similarly indicates a stable condition along the tunnel sidewall, whereas Sections 4–6 exhibit substantially lower SSR values associated with the pillar, pillar–gob transition, and gob/face region.

ACCEPTED MANUSCRIPT

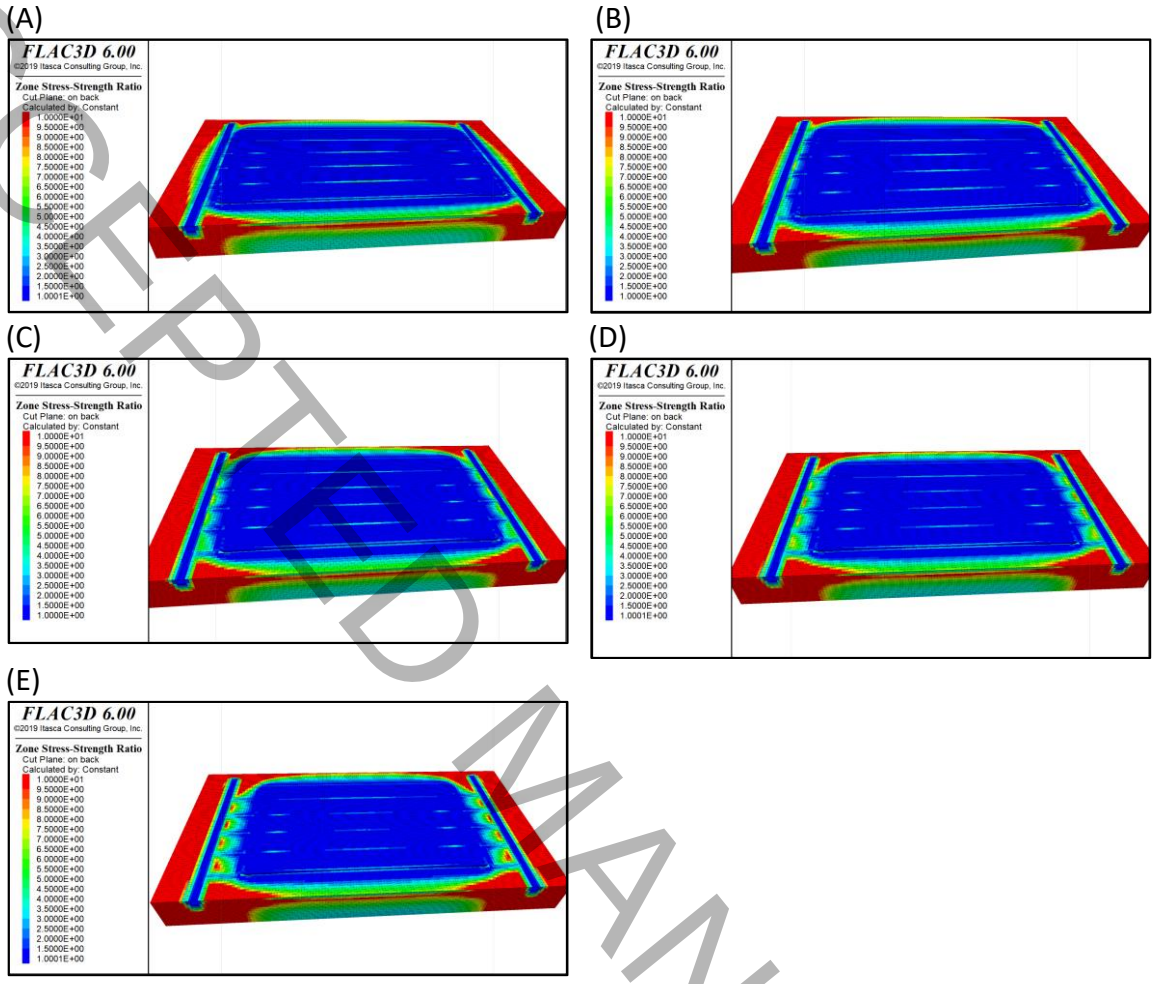

Fig. 13. Stress–strength ratio (SSR) contour maps of the C1W4 panel for different pillar widths ((A)–(E): 4, 6, 8, 10, and 12 m pillar configurations)

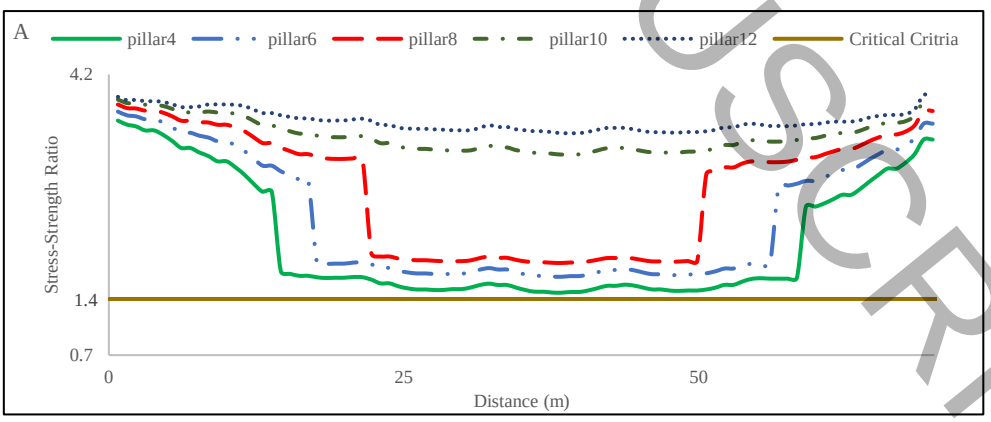

ACCEPTED MANUSCRIPT

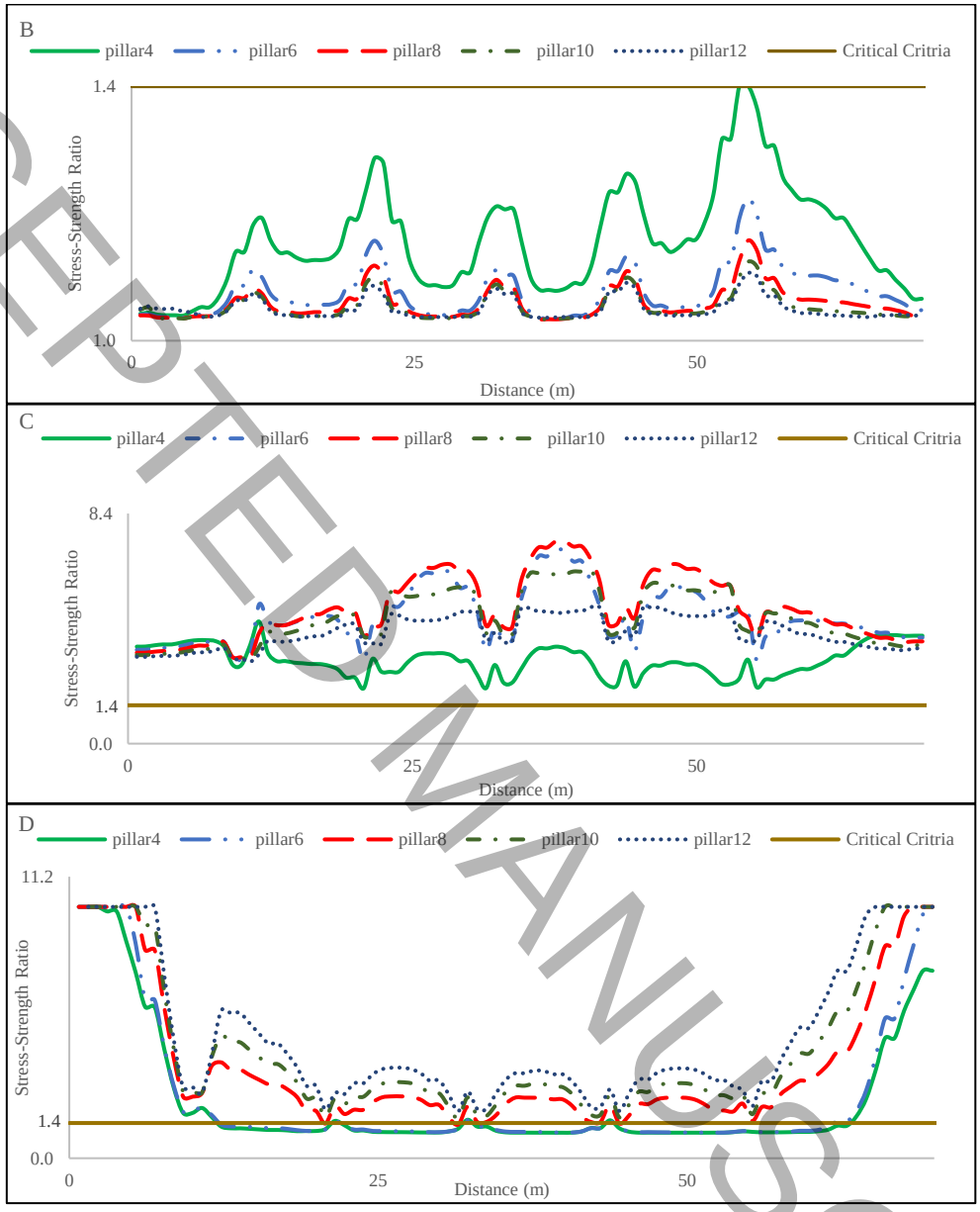

ACCEPTED MANUSCRIPT

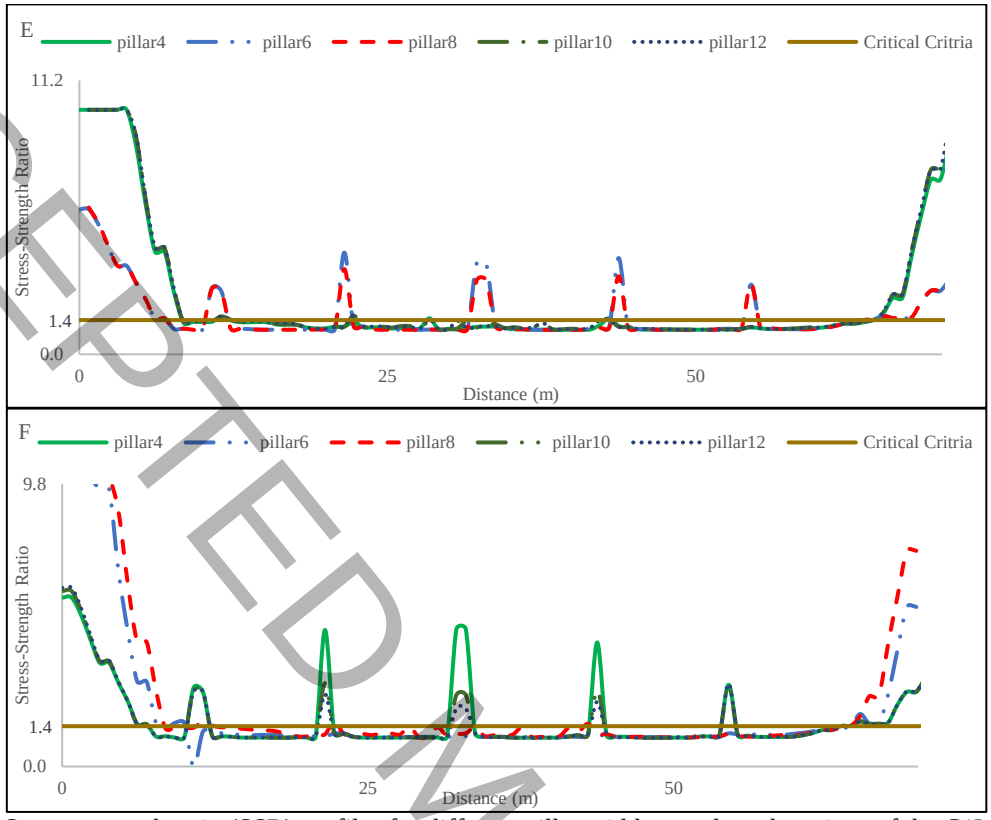

Fig. 14. Stress–strength ratio (SSR) profiles for different pillar widths at selected sections of the C1W4 panel ((A)–(F): tunnel wall on the intact-coal side, tunnel roof, tunnel wall on the gob side, pillar center between the tunnel and gob, pillar edge adjacent to the gob, and gob center)

The evolution of SSR at the pillar centerline during progressive extraction is shown in Fig. 15. This analysis provides a temporal perspective on the changes identified spatially in Fig. 14. For the 4 m pillar, the SSR decreases below 1.4 after the first caving stage, indicating that the pillar centerline approaches or enters an unfavourable strength condition at an early stage of extraction. A similar reduction occurs for the 6 m configuration, for which the SSR also falls below the adopted criterion after the first caving stage.

The 8 m pillar exhibits an intermediate response. Its SSR remains close to the reference value of 1.4 throughout the extraction sequence, indicating a condition near the adopted stability limit. The wider 10 and 12 m pillars maintain SSR values above 1.4 during the simulated caving stages, indicating a greater strength margin against the mining-induced stress state.

The progressive reduction in SSR for the narrower pillars reflects the increasing influence of load transfer from the extracted zone and the associated concentration of stress within the remaining coal. The results therefore demonstrate that pillar width has a substantial influence on the available stability margin, even though its effect on the overall peak vertical stress magnitude is relatively limited. In particular, the 4 and 6 m configurations exhibit insufficient SSR margins, the 8 m configuration represents a transitional or marginal condition, and the 10 and 12 m configurations maintain SSR values consistent with the adopted stability criterion.

ACCEPTED MANUSCRIPT

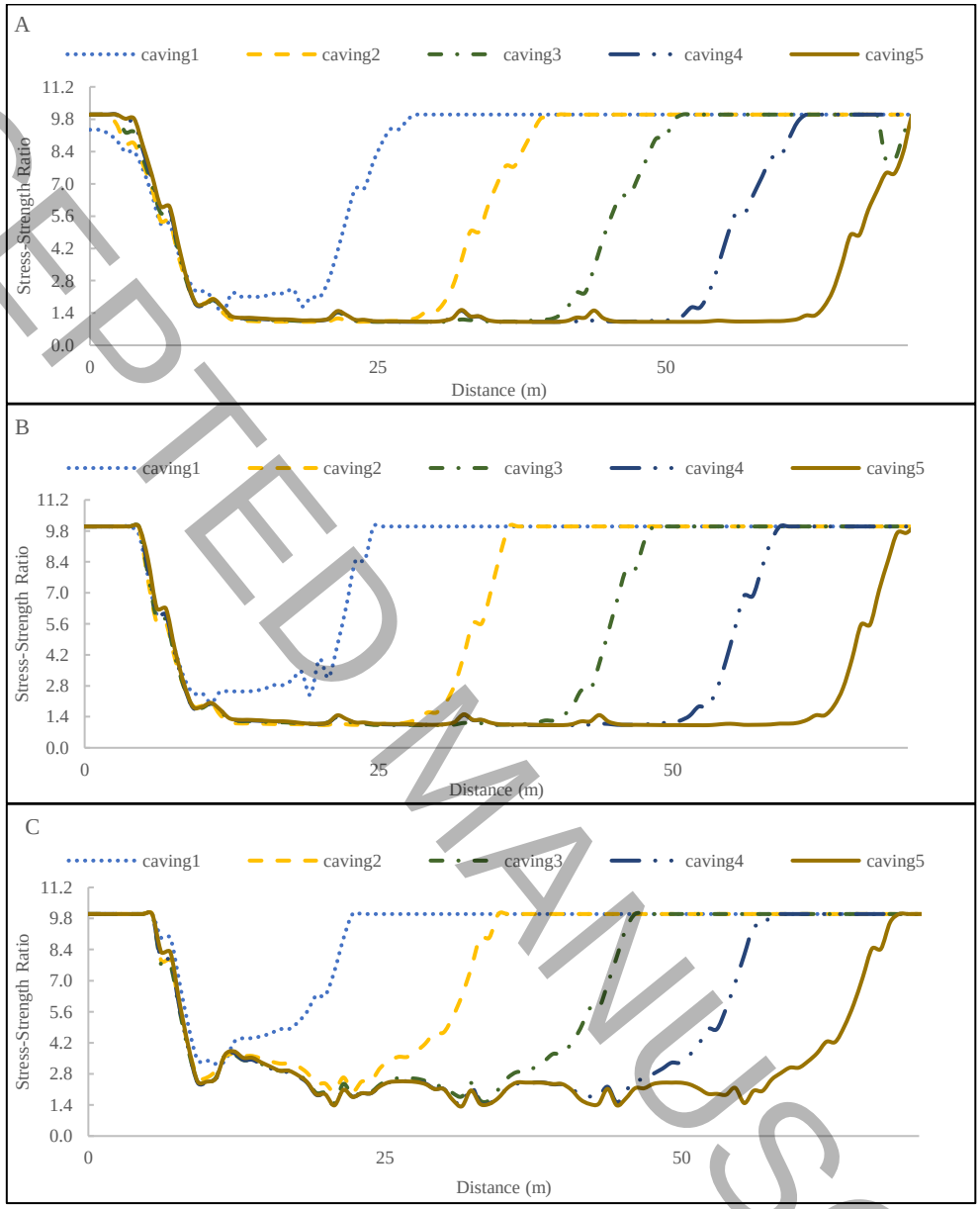

ACCEPTED MANUSCRIPT

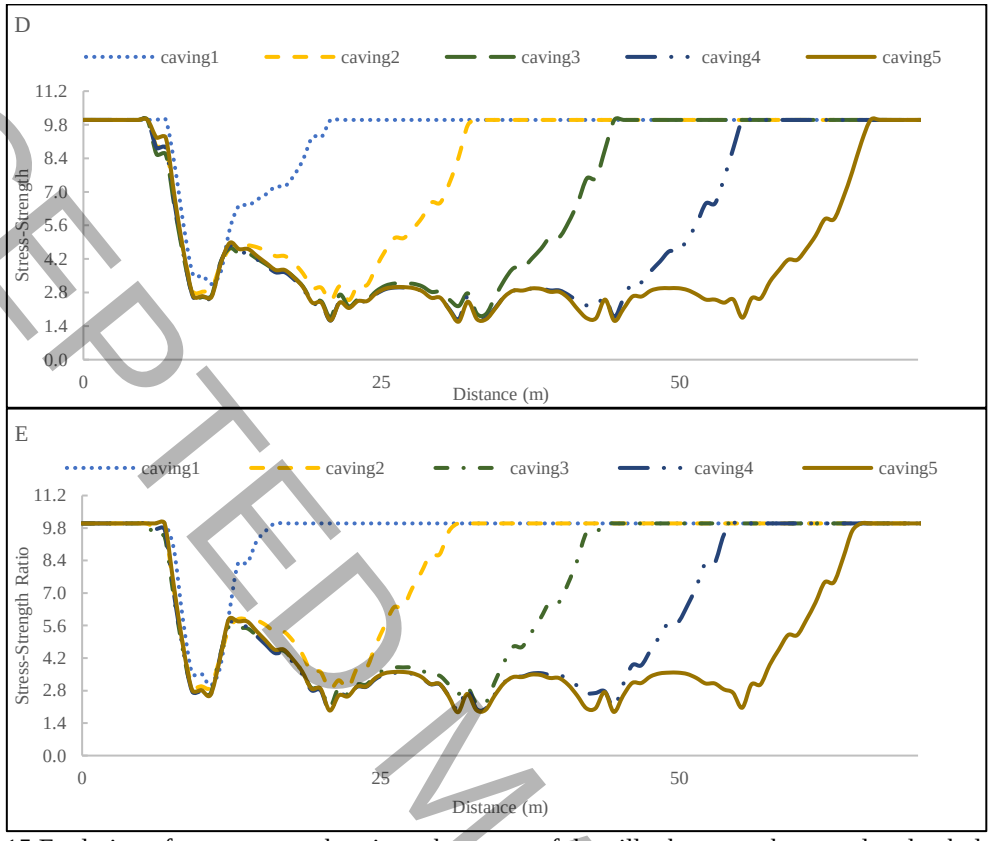

Fig. 15 Evolution of stress–strength ratio at the center of the pillar between the tunnel and gob during progressive mining for different pillar widths ((A)–(E): 4, 6, 8, 10, and 12 m pillar configurations)

4.5. Plastic Zone Development

The evolution of plasticity during progressive caving provides further insight into the mechanisms governing pillar and roadway response. The numerical results indicate that shear yielding constitutes the predominant failure mechanism within the modeled ground mass. In contrast, plastic deformation around the tunnel roof and sidewalls remains relatively localized, whereas more evident shear yielding develops near the tunnel floor, in agreement with the tendency for floor heave observed in the field.

A pronounced dependence of the plastic-zone extent on pillar width is evident in Fig. 16. For the 4 and 6 m configurations, the yielded region progressively expands across a large portion of the pillar, leaving little or no intact load-bearing core. The 8 m pillar exhibits an intermediate response, with plasticity extending farther into the pillar than in the wider configurations. By comparison, the 10 and 12 m pillars retain a comparatively well-defined central region with limited plastic development, while yielding is concentrated mainly toward their outer portions adjacent to the excavation and gob.

These results demonstrate that increasing pillar width changes not only the magnitude of deformation but also the internal distribution of yielding. The narrowest pillars are characterized by extensive plasticization across their cross-section, indicating a substantially reduced capacity to preserve an intact load-bearing core. Wider pillars, particularly those with widths of 10 and 12 m, retain a central less-yielded region surrounded by localized peripheral plasticity. This configuration provides a more favourable load-bearing structure during successive stages of longwall advance.

ACCEPTED MANUSCRIPT

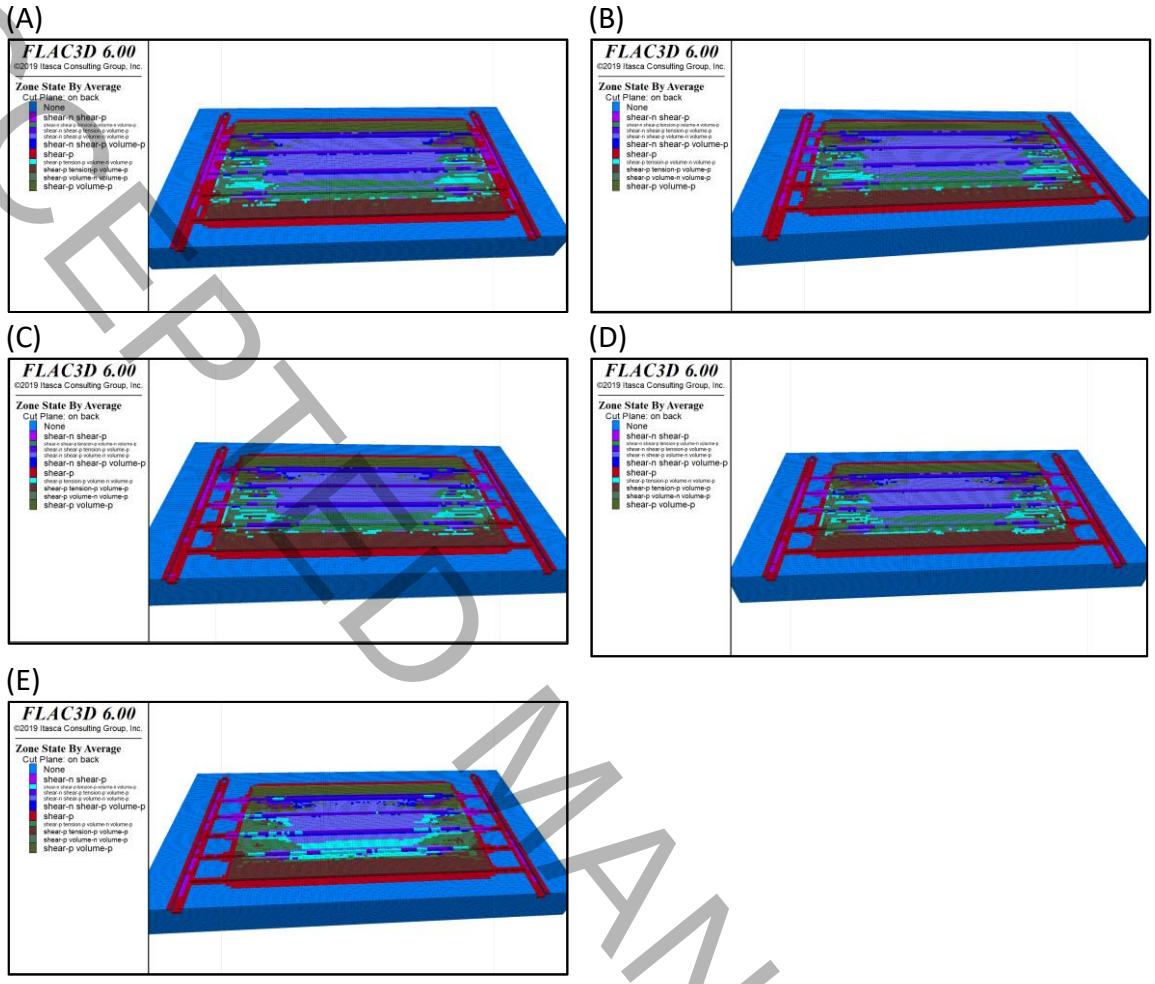

Fig. 16 Plastic-zone development under five successive caving steps for different pillar widths ((A)–(E): 4, 6, 8, 10, and 12 m)

4.6. Support-System Performance

The response of the roadway support system was examined in terms of support displacement and the interaction between axial/thrust loading and bending or shear resistance. The calculated maximum displacement of the support system decreased systematically as pillar width increased, from approximately 18 mm for the 4 m configuration to 13, 10, 8, and 6 mm for pillar widths of 6, 8, 10, and 12 m, respectively.

The load–moment interaction results shown in Figs. 17 and 18 indicate a clear distinction between the narrow- and wide-pillar cases. For the 10 and 12 m configurations, all calculated demand points remained inside the corresponding resistance envelopes, and neither the steel sets nor the shotcrete exhibited yielding. The support response therefore remained within the specified structural limits throughout the modeled extraction stages.

The 8 m configuration produced an intermediate response. Although the shotcrete lining remained within its stable response domain, several localized points associated with the steel sets indicated instability. The situation became more pronounced for the 4 and 6 m configurations, where unstable response points were identified in both support components. In these cases, the bending response of the shotcrete also indicated instability, accompanied by multiple critical locations in the steel sets (Fig. 18).

ACCEPTED MANUSCRIPT

The maximum calculated support pressure was approximately 30 MPa. Within the investigated configurations, this demand remained below the adopted structural capacity for pillar widths of 10 m and greater. The progressive reduction in support displacement, together with the load–moment interaction results, therefore indicates that increasing pillar width substantially alleviates the mechanical demand imposed on the roadway support system.

Overall, the numerical results show that the 10 and 12 m pillar configurations maintained stable support behavior during the simulated advance of the C1W4 panel. No support failure or instability was identified for either configuration. These results are consistent with the stable response obtained for the surrounding roof and sidewall regions and indicate that the existing maingate and tailgate support arrangements can accommodate the ground response associated with these wider pillars.

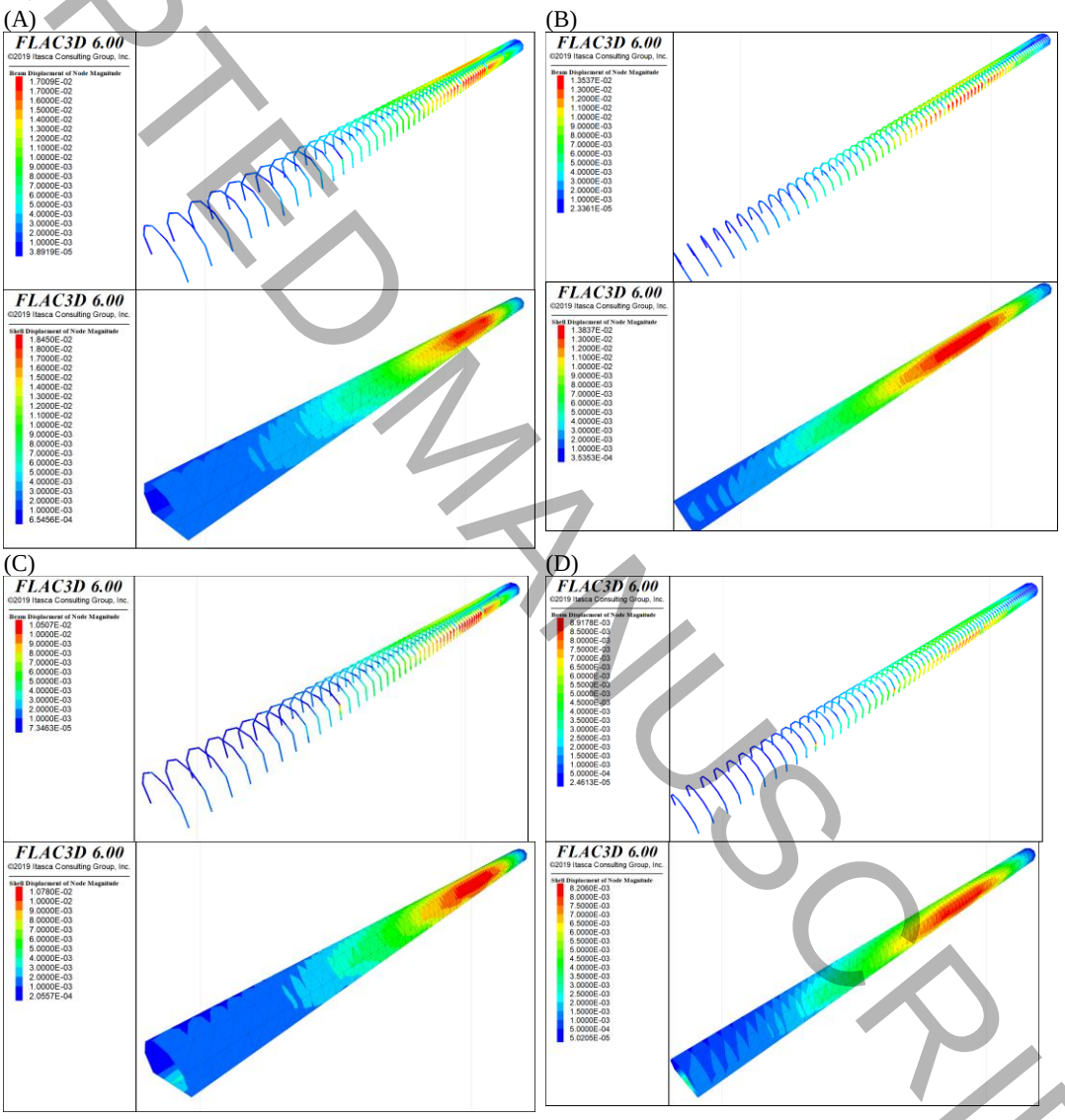

ACCEPTED MANUSCRIPT

(E)

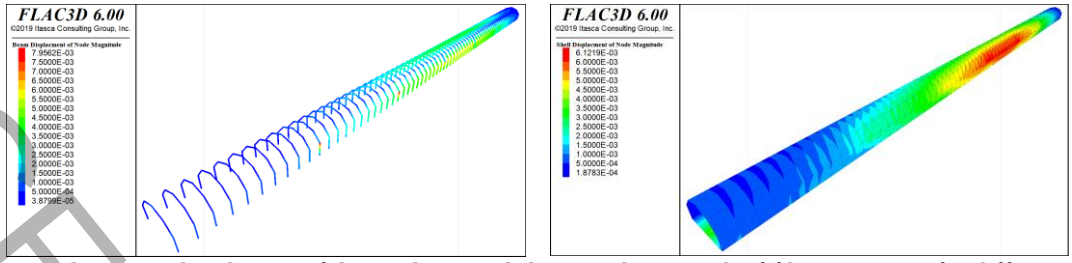

Fig. 17 Displacement distribution of the steel sets and shotcrete lining at the fifth caving step for different pillar widths ((A)–(E): 4, 6, 8, 10, and 12 m)

(A)

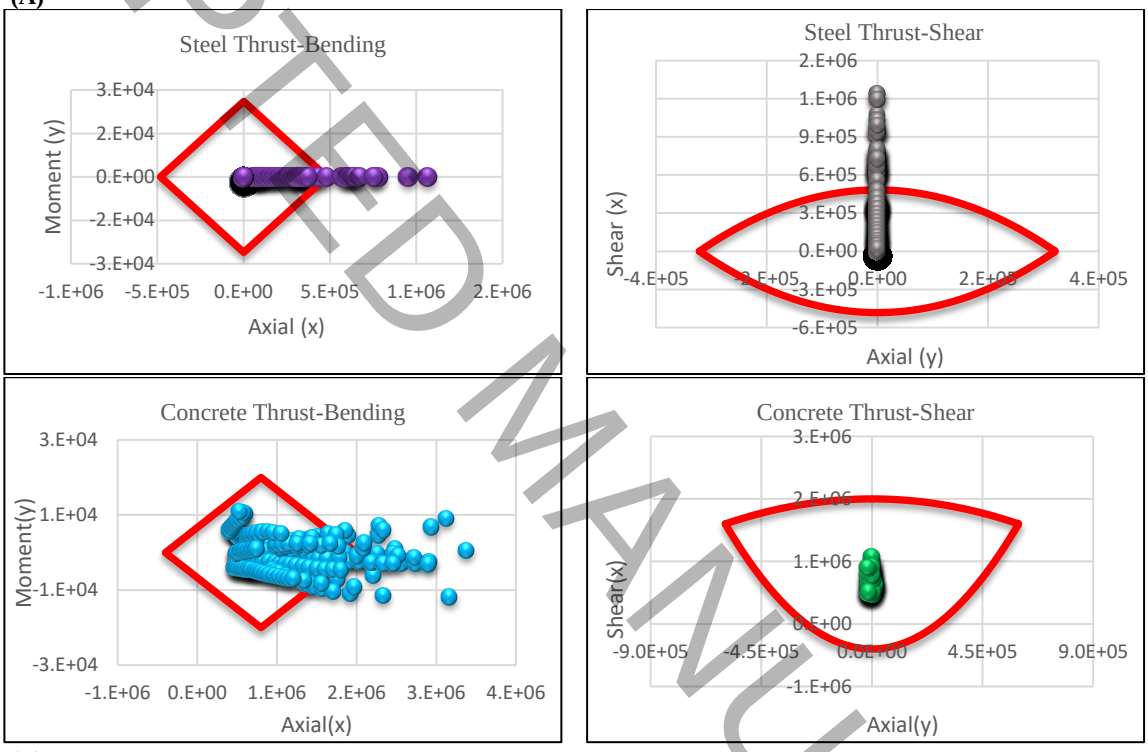

(B)

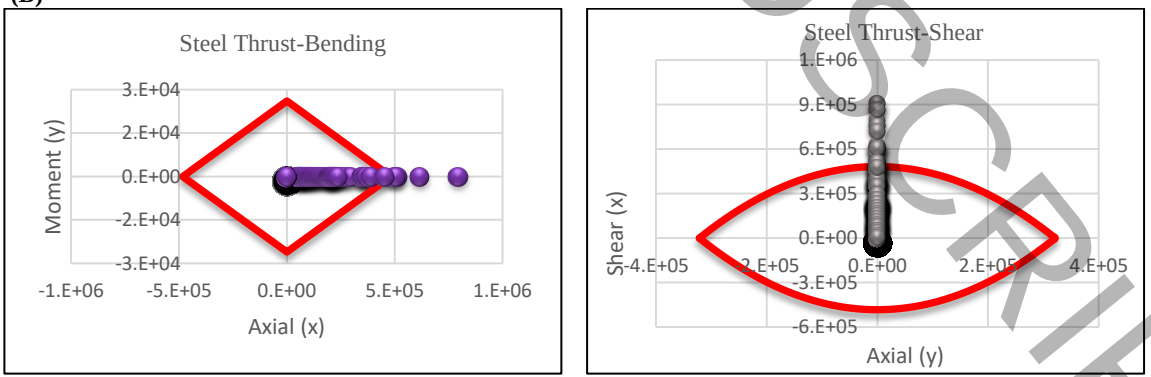

ACCEPTED MANUSCRIPT

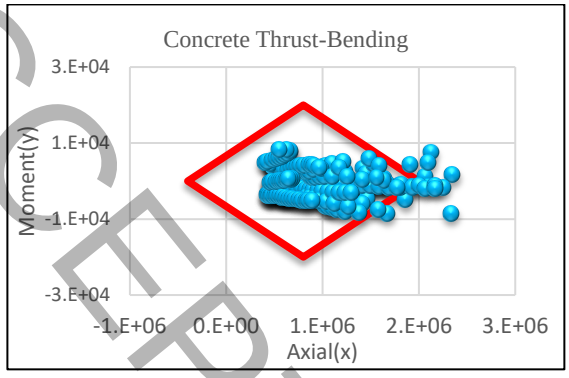

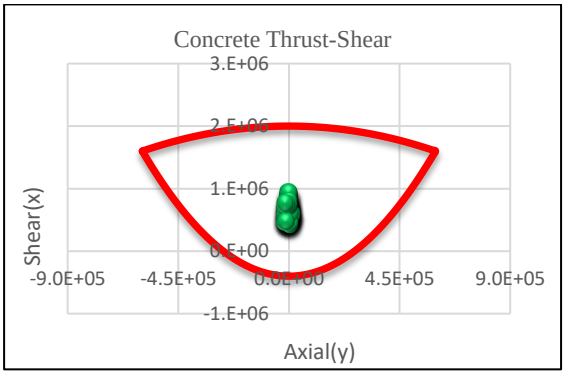

(C)

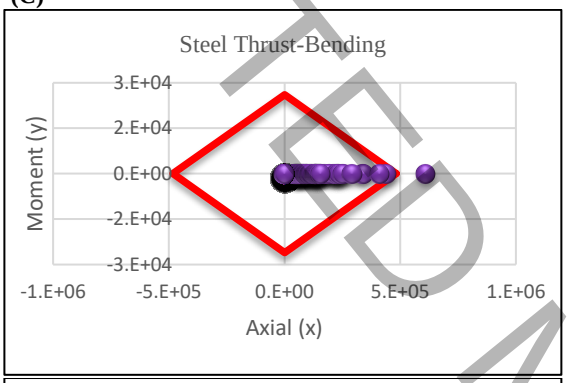

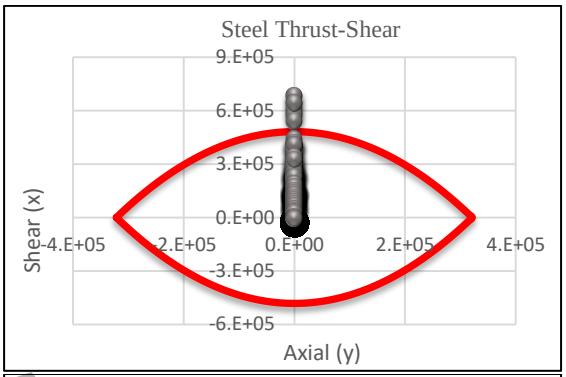

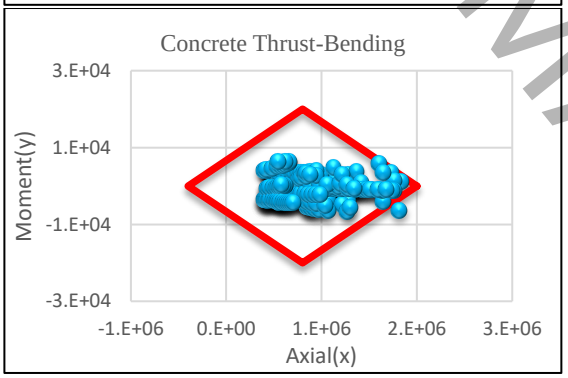

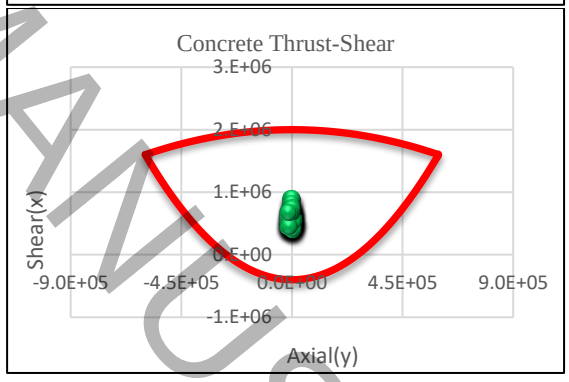

(D)

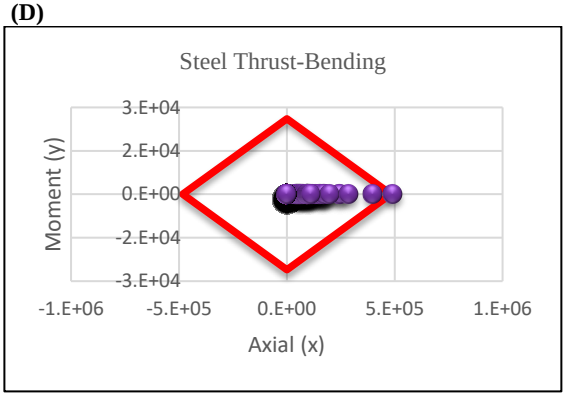

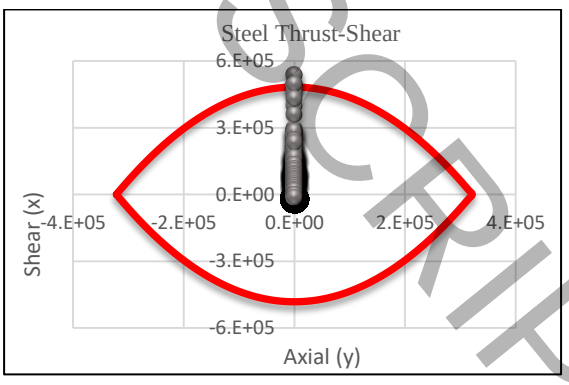

ACCEPTED MANUSCRIPT

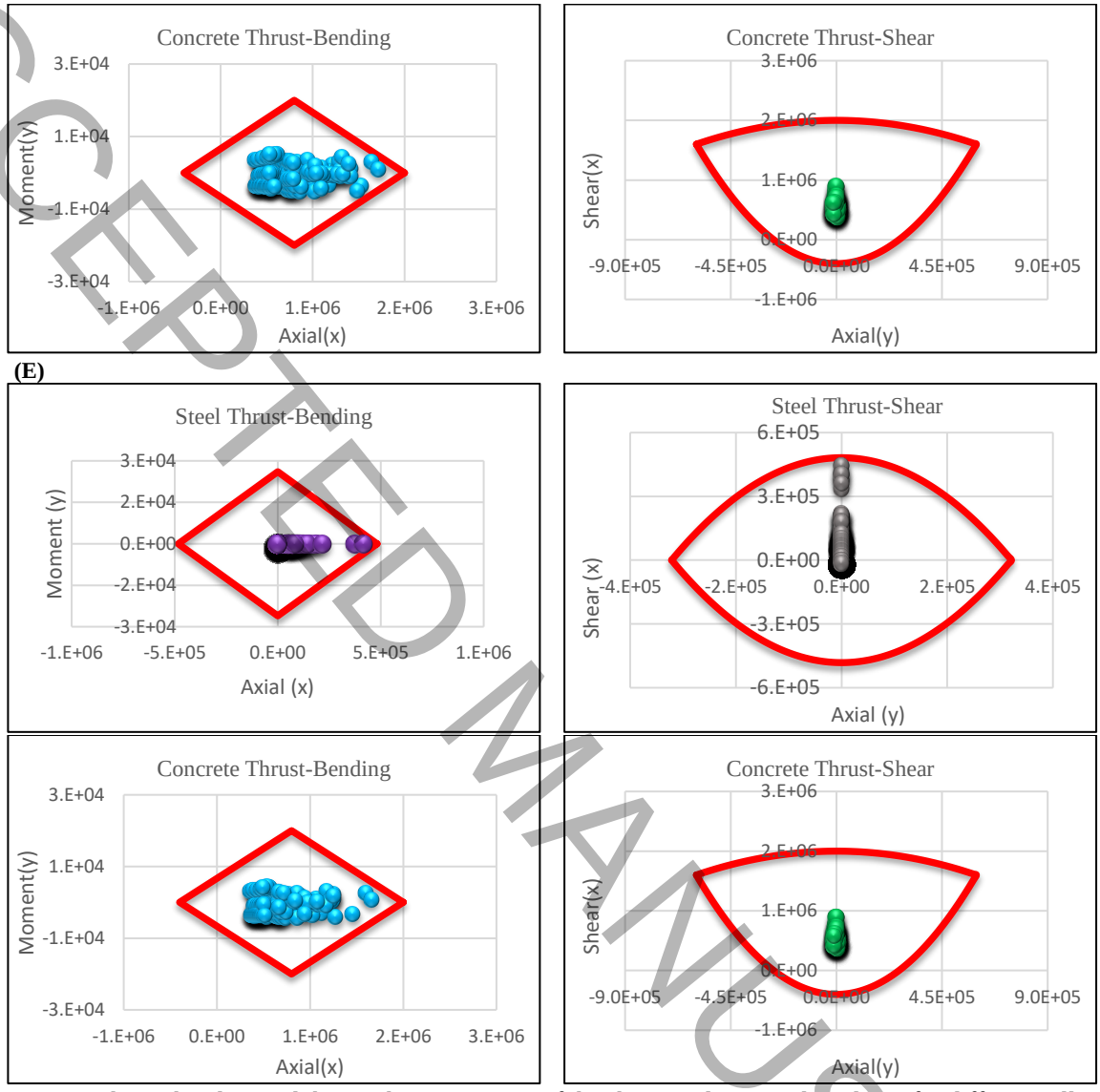

Fig. 18 Thrust–bending and thrust–shear responses of the shotcrete lining and steel sets for different pillar widths after the fifth caving step (pillar widths: 4, 6, 8, 10, and 12 m)

4.7. Integrated Mechanical Interpretation

Taken together, the numerical results demonstrate that the mechanical response of the C1W4 panel is controlled by the coupled behavior of the caved zone, panel pillars, and roadway support system. As the longwall face advances, progressive roof caving and gob compaction modify the surrounding stress field and promote the development of abutment stresses ahead of the face. Part of the transferred load is subsequently accommodated by the panel pillars and the ground surrounding the adjacent gate roadways. The resulting response is therefore determined by the combined stiffness and deformation characteristics of these interacting components rather than by any single stability indicator.

Pillar width plays a central role in this interaction. Narrow pillars undergo greater deformation and more extensive plastic yielding, while also imposing higher mechanical demands on the roadway support system.

ACCEPTED MANUSCRIPT

ACCEPTED MANUSCRIPT

Increasing the width reduces the extent of yielding and deformation and allows a larger portion of the pillar to remain within a less-yielded load-bearing state. However, increasing pillar width also increases the amount of coal retained in the pillar and consequently affects extraction efficiency. Within the range investigated in this study, the 8 m configuration represents a transitional condition, whereas the 10 m configuration provides a more stable mechanical response while retaining a comparatively reasonable pillar dimension.

From a modeling perspective, the numerical framework reproduced the principal mechanisms observed during progressive extraction, including:

- nonlinear compression and compaction of the gob;
- redistribution and concentration of mining-induced stresses;
- progressive development of plastic yielding within the coal pillars; and
- interaction between ground deformation and the roadway support system.

The combined interpretation of these responses provides a more comprehensive assessment of pillar and roadway behavior than any individual parameter considered separately. In particular, the consistency between stress redistribution, displacement, shear-strain development, SSR, plastic-zone extent, and support response provides the mechanical basis for distinguishing the different pillar-width configurations. The numerical predictions are further evaluated against field monitoring data in the following section to assess the capability of the model to reproduce the observed ground response.

5. Model Validation and Discussion

The predictive performance of the three-dimensional FLAC3D model was assessed using field measurements of roof displacement collected from extensometers installed along the maingate of the C1W4 panel. Roof extensometer is a commonly used monitoring technique for quantifying strata movement in underground excavations and is capable of resolving displacement at the millimetre scale. At Parvadeh IV, the monitoring instruments were positioned at the entrances of the X-cuts along the maingate. Because successive extraction stages correspond to approximately 10 m of longwall advance and each X-cut is approximately 1 m wide, the resulting spacing between adjacent monitoring locations is about 11 m. Six corresponding locations were therefore incorporated into the numerical model, allowing the calculated vertical displacement histories to be compared directly with the available field records.

Figure 19 presents the measured and simulated roof-displacement histories for the six monitoring locations (A–F). The comparison encompasses 11 operational states, beginning with the pre-mining condition and continuing through the subsequent excavation and caving stages. A total of 66 paired displacement observations were consequently available for quantitative assessment of the numerical predictions.

Two statistical measures, the root mean square error (RMSE) and mean absolute percentage error (MAPE), were used to characterize the prediction error. Considering all 66 observations, the calculated RMSE was 1.60 mm, while the MAPE was 22.17%. These error levels, together with the similar evolution of the measured and calculated displacement histories, indicate that the model captures the principal magnitude and progression of roof deformation under the simulated mining conditions. The remaining differences at individual monitoring locations are reasonably attributable to local variations in geological and mechanical conditions, as well as the necessary simplifications associated with numerical representation of the caved material. Thus, the model provides a sufficiently consistent representation of the maingate roof response for engineering-level interpretation.

The correlation between the two datasets was additionally examined using the coefficient of determination. An R^2 of 0.8949 was obtained from the complete set of 66 observations, demonstrating a strong correspondence in the overall variation of simulated and measured displacement. The scatter comparison in Fig. 20, together with the 1:1 reference line, further illustrates this relationship. Nevertheless, the MAPE of 22.17% indicates that the agreement should not be interpreted as an exact point-by-point reproduction. This is particularly relevant because the measured displacements are relatively small, making percentage-based errors more sensitive to minor absolute differences. Accordingly, the principal significance of the validation lies in the model's ability to reproduce the overall deformation pattern and displacement range rather than every individual measurement.

A systematic tendency for the numerical model to predict somewhat smaller displacements than those measured in the field can also be identified. Several aspects of the numerical formulation may contribute to this behavior. The elastic-perfectly plastic Mohr–Coulomb formulation provides a practical representation of the principal stress–deformation response but does not explicitly account for time-dependent deformation, progressive deterioration of post-peak rock-mass strength, or the development of discrete localized fractures. Furthermore, the double-yield parameters adopted for the gob describe an averaged compaction response and therefore cannot fully represent the spatial variability that may exist within an actual caved zone. The combined effect of these assumptions can result in a lower calculated roof deformation relative to field observations.

The validation was not restricted to statistical comparison of displacement measurements. Additional evidence was obtained by examining whether the predicted mechanical response was compatible with observed mine behavior. During the investigated operating period, no major instability was reported in the C1W4 maingate, which is consistent with the generally acceptable roof and sidewall response obtained from the numerical analysis. The 8 m pillar, however, retains a smaller mechanical margin according to the combined stability indicators than the 10 and 12 m configurations.

Field observations reported for Parvadeh IV also include localized pillar spalling and associated increases in permeability. The numerical simulations reproduce a mechanically consistent form of this behavior through the development of shear-dominated plastic regions within the narrower pillars, particularly for the 4 and 6 m configurations. Similarly, the concentration of plastic deformation predicted near the floor corresponds with the general tendency for floor heave reported in the ventilation and haulage roadways. These qualitative consistencies provide additional support for the interpretation of the dominant deformation and yielding mechanisms identified by the model.

The final assessment of pillar performance was based on the combined interpretation of four groups of mechanical indicators: stress redistribution and displacement, critical shear strain, plastic-zone development, and stress–strength ratio (SSR). Considering these indicators together highlights the strong influence of pillar width on the mechanical response of the panel. In the 4 m configuration, the shear strain at the pillar center exceeds the critical value of $\gamma c = 0.0062$, while the plastic region extends substantially across the pillar and the SSR decreases below the adopted criterion of 1.4. The combined response therefore identifies this configuration as mechanically unfavourable.

The 6 m pillar shows an improvement relative to the 4 m case, particularly with respect to the shear-strain criterion, which remains below the critical threshold at the pillar center. Nevertheless, the extensive development of plasticity and the SSR response indicate a limited stability margin under the modeled loading conditions. The 8 m configuration occupies an intermediate position between these two responses. Its central shear strain remains below γc and the plastic zone does not completely traverse the pillar; however, the corresponding SSR remains close to the adopted threshold of 1.4. It can therefore be regarded as a transitional configuration rather than one providing the same stability margin as the wider pillars.

The 10 and 12 m configurations show a distinctly more controlled mechanical response. In both cases, SSR values remain above 1.4, plastic yielding is concentrated mainly in the peripheral portions of the pillars, and the resulting deformation remains comparatively limited. These results are also consistent with the more favourable support response identified in Section 4.6. Taken together, the different indicators show that the transition from marginal to more stable behavior occurs within the range between 8 and 10 m rather than at a single sharply defined pillar width.

An additional consideration is that short-term roadway stability does not necessarily provide a complete measure of the long-term suitability of a pillar configuration. The extent of pillar damage and associated fracture development can influence permeability within the coal mass. Consequently, narrower pillars, even where roadway deformation remains manageable, may provide more extensive pathways for fluid migration through damaged coal. Under deeper or otherwise more demanding future mining conditions, such changes in permeability could also become relevant to gas migration and spontaneous-combustion-related operational risks. These implications should therefore be considered alongside the immediate geomechanical response when selecting pillar dimensions.

ACCEPTED MANUSCRIPT

For the geological, geometric, and loading conditions represented in the present C1W4 model, the combined numerical and field evidence supports the use of a 10 m pillar as a mechanically stable configuration among the investigated alternatives, while the 12 m pillar provides a comparable stable response at the expense of retaining more coal. The 8 m configuration remains transitional and has a smaller mechanical margin. Thus, the results should be interpreted specifically within the modeled conditions rather than as a universal pillar-width criterion for other mining settings.

Overall, the agreement between the numerical predictions and field measurements, together with the consistency of the predicted deformation and yielding mechanisms with reported mine behavior, supports the applicability of the developed FLAC3D model for the present case study. The validated model can subsequently be employed for additional parametric investigations of pillar dimensions and ground-control conditions, provided that changes in geological setting, stress regime, and mining geometry are appropriately incorporated.

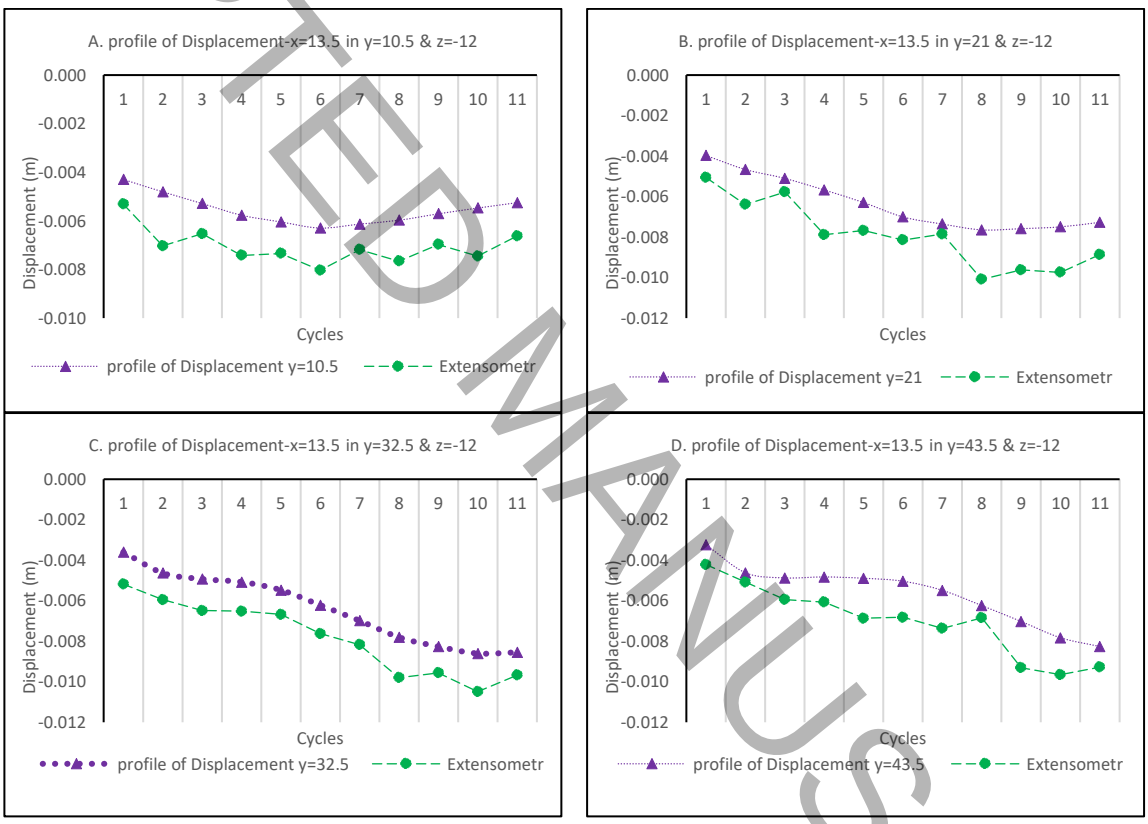

ACCEPTED MANUSCRIPT

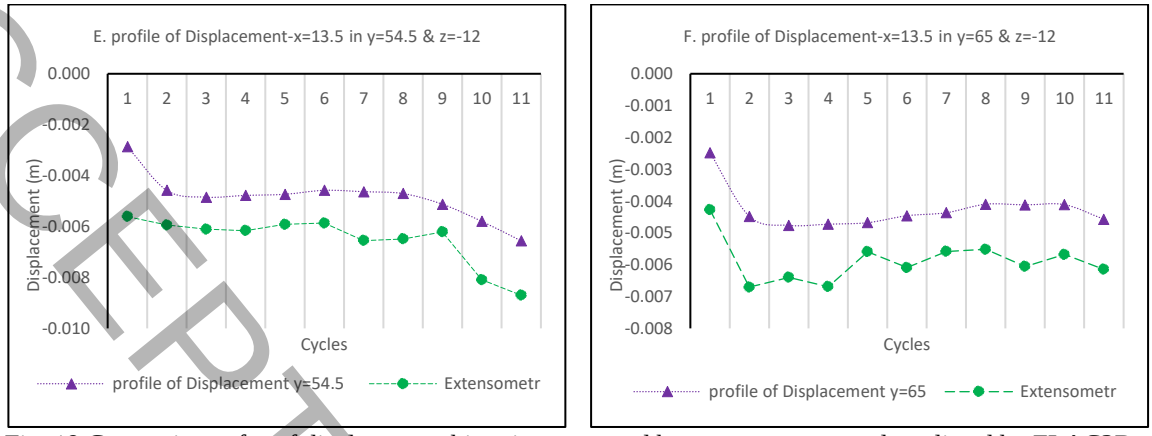

Fig. 19 Comparison of roof displacement histories measured by extensometers and predicted by FLAC3D at six monitoring locations during the analyzed operational stages

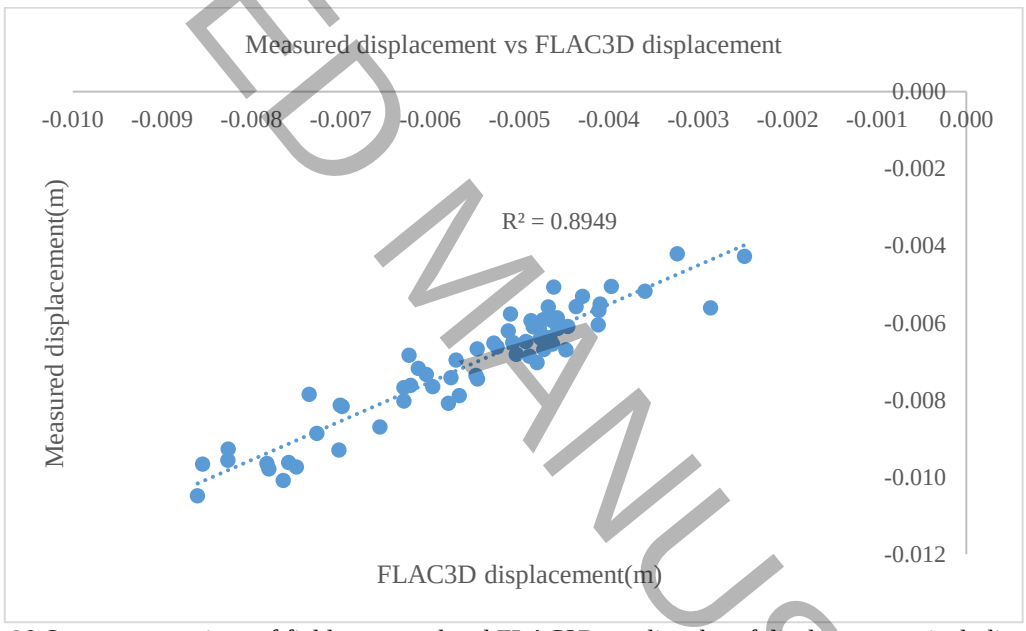

Fig. 20 Scatter comparison of field-measured and FLAC3D-predicted roof displacements, including the 1:1 reference line

6. Conclusions

A three-dimensional FLAC3D model was developed to examine the mechanical response of gate roadways and panel pillars during progressive longwall extraction in the C1W4 panel of the Parvadeh IV coal mine. Pillar widths of 4, 6, 8, 10, and 12 m were investigated using a combined assessment of mining-induced stress redistribution, ground displacement, critical shear strain, plastic-zone development, support response, and stress–strength ratio (SSR). The numerical predictions were also evaluated against roof-extensometer measurements and available field observations. The resulting agreement between numerical and field responses supports the applicability of the model for interpreting the geomechanical behavior of the investigated panel.

ACCEPTED MANUSCRIPT

The numerical results demonstrate a systematic relationship between pillar width and the mechanical response of the roadway–pillar system. Reduction in pillar width is accompanied by greater stress concentration, increased pillar deformation, more extensive plastic yielding, and lower SSR values. The associated increase in support demand becomes particularly evident for the narrower configurations. These results indicate that pillar performance cannot be adequately characterized by a single parameter; rather, the combined interpretation of stress, deformation, yielding, SSR, and support behavior provides a more representative basis for distinguishing the investigated configurations.

The 4 and 6 m pillars exhibited the least favorable mechanical responses. The 4 m configuration was characterized by extensive plasticization, critical shear strain exceeding the adopted threshold at the pillar center, and SSR values below the specified stability criterion. The 6 m pillar showed an improved shear-strain response but still developed substantial plastic yielding and an unfavorable SSR response. The 8 m configuration exhibited intermediate behavior: its central shear strain remained below the critical value and the plastic zone did not completely penetrate the pillar, but the SSR remained close to the adopted limit of 1.4. It was therefore identified as a transitional configuration with a relatively limited mechanical margin.

The 10 and 12 m configurations maintained a more controlled mechanical response throughout the simulated extraction stages. Both retained comparatively substantial less-yielded cores, restricted plastic deformation mainly to peripheral regions, and maintained SSR values above 1.4. Their associated support responses also remained within the adopted structural limits. Considering the complete set of stability indicators, the transition from marginal to more stable behavior occurs within the 8–10 m interval under the geological and loading conditions represented in the model.

Among the investigated alternatives, the 10 m pillar provides a mechanically stable and operationally suitable configuration for the modeled C1W4 conditions, while the 12 m pillar exhibits a similarly stable response with a greater amount of coal retained in the pillar. The 10 m result should not, however, be interpreted as an exact critical or universally optimum pillar width. Because widths between 8 and 10 m were not explicitly simulated, additional analyses using smaller increments are required to determine the precise location of the stability transition and to investigate the trade-off between mechanical performance and coal recovery more closely.

The field-validation results further support the use of the numerical framework for engineering interpretation. Comparison of 66 paired displacement observations from six extensometer locations over 11 operational stages produced an RMSE of 1.60 mm, a MAPE of 22.17%, and an R^2 of 0.8949. Although the model generally underestimated the measured roof displacement, it reproduced the principal displacement trend and magnitude range with reasonable consistency. The remaining differences are likely related to geological heterogeneity, simplifications in the representation of the rock mass and gob, and the limitations of the adopted constitutive formulation in reproducing time-dependent and localized post-peak deformation.

Several limitations should be considered when extending these findings beyond the present case study. Uncertainty in rock-mass properties, the simplified representation of geological layering, the adopted stress conditions, and the omission of explicit mechanical interaction with adjacent panels may affect the calculated response. In addition, the elastic-perfectly plastic Mohr–Coulomb formulation does not explicitly represent progressive strain-softening or localized fracture development. Future work should therefore include mesh-sensitivity studies, systematic uncertainty and parameter analyses, more advanced constitutive formulations, refined simulations within the 8–10 m interval, and additional field-based calibration.

Finally, the present investigation is primarily concerned with the geomechanical performance of the roadway–pillar system. Other factors that may influence pillar-dimension selection, including coal recovery, permeability evolution, gas migration, and spontaneous-combustion risk, were not explicitly coupled with the present stability analysis. An integrated assessment incorporating these operational and safety considerations would provide a broader basis for pillar-dimension optimization in future longwall developments at Parvadeh IV and comparable coal-mining environments.

Reference

1. Sherizadeh T, Kulatilake PH (2016). Assessment of roof stability in a room and pillar coal mine in the

ACCEPTED MANUSCRIPT

US using three-dimensional distinct element method. Tunnelling and Underground Space Technology, 59, 24-37.
2. Coggan J, Gao F, Stead D, Elmo D (2012). Numerical modelling of the effects of weak immediate roof lithology on coal mine roadway stability. International journal of coal geology, 90, 100-09.
3. Singh G, Singh U (2009). A numerical modeling approach for assessment of progressive caving of strata and performance of hydraulic powered support in longwall workings. Computers and Geotechnics, 36(7), 1142-56.
4. Singh* GSP, Singh UK (2011). Assessment of goaf characteristics and compaction in longwall caving. Mining Technology, 120(4), 222-32.
5. Bai Q, Tu S, Wang F, Zhang C (2017). Field and numerical investigations of gateroad system failure induced by hard roofs in a longwall top coal caving face. International Journal of Coal Geology, 173, 176-99.
6. Yavuz H (2004). An estimation method for cover pressure re-establishment distance and pressure distribution in the goaf of longwall coal mines. International Journal of Rock Mechanics and Mining Sciences, 41(2), 193-205.
7. Gale, W. J., & Blackwood, R. L. (1987, June). Stress distributions and rock failure around coal mine roadways. In International Journal of Rock Mechanics and Mining Sciences & Geomechanics Abstracts (Vol. 24, No. 3, pp. 165-173). Pergamon.
8. Toraño J, Díez RRg, Cid JR, Barciella MC (2002). FEM modeling of roadways driven in a fractured rock mass under a longwall influence. Computers and Geotechnics, 29(6), 411-31.
9. Badr, S., Mendoza, R., Kieffer, S., Salamon, M. D. G., & Ozbay, M. U. (2003, August). Numerical modelling of longwalls in deep coal mine. In Proceedings of the 22nd Conference on Ground Control in Mining (pp. 37-43). West Virginia University, Morgantown, West Virginia.
10. Zhang J, Shen B (2004). Coal mining under aquifers in China: a case study. International Journal of Rock Mechanics and Mining Sciences, 41(4), 629-39.
11. Peng S (2019). Longwall mining: CRC Press.
12. Najafi, M., Jalali, S. M. E., Sereshki, F., & Yarahmadi, B. A. (2010). Estimation of the load distribution on the chain pillars of the mechanized longwall panels in Tabas coal mine using numerical method.
13. Shabanimashcool M, Li CC (2012). Numerical modelling of longwall mining and stability analysis of the gates in a coal mine. International Journal of Rock Mechanics and Mining Sciences, 51, 24-34.
14. Kulatilake P, Wu Q, Yu Z, Jiang F (2013). Investigation of stability of a tunnel in a deep coal mine in China. International Journal of Mining Science and Technology, 23(4), 579-89.
15. Abdellah W, Raju G, Mitri HS, Thibodeau D (2014). Stability of underground mine development intersections during the life of a mine plan. International Journal of Rock Mechanics and Mining Sciences, 72, 173-81.
16. Bai J-b, Shen W-l, Guo G-l, Wang X-y, Yu Y (2015). Roof deformation, failure characteristics, and preventive techniques of gob-side entry driving heading adjacent to the advancing working face. Rock Mechanics and Rock Engineering, 48(6), 2447-58.
17. Rezaei M, Hossaini MF, Majdi A (2015). Development of a time-dependent energy model to calculate the mining-induced stress over gates and pillars. Journal of Rock Mechanics and Geotechnical Engineering, 7(3), 306-17.
18. Jiang L, Zhang P, Chen L, Hao Z, Sainoki A, Mitri HS, et al (2017). Numerical approach for goaf-side entry layout and yield pillar design in fractured ground conditions. Rock Mechanics and Rock Engineering, 50(11), 3049-71.
19. Yang S-Q, Chen M, Jing H-W, Chen K-F, Meng B (2017). A case study on large deformation failure mechanism of deep soft rock roadway in Xin'An coal mine, China. Engineering Geology, 217, 89-101.
20. Tulu I, Esterhuizen G, Gearhart D, Klemetti T, Mohamed K, Su D (2018). Analysis of global and local stress changes in a longwall gateroad. International journal of mining science and technology, 28(1), 127-35.
21. Ozdogan MV, Yenice H, Gönen A, Karakus D (2018). Optimal support spacing for steel sets: Omerler

ACCEPTED MANUSCRIPT

underground coal mine in Western Turkey. International Journal of Geomechanics, 18(2), 05017003.
22. Damghani M, Rahmannejad R, Najafi M (2019). Evaluation of the effect of coal seam dip on stress distribution and displacement around the mechanized longwall panel. Journal of Mining Science, 55(5), 733-42.
23. Wang X, Lai J, Garnes RS, Luo Y (2019). Support system for tunnelling in squeezing ground of Qingling-Daba mountainous area: a case study from soft rock tunnels. Advances in Civil Engineering, (1), 8682535.
24. Boothukuri VR, Bhattacharjee RM, Panigrahi DC, Benerjee G (2019). Impact of geo technical factors on strata behavior in longwall panels of Godavari Valley coal field-a case study. International Journal of Mining Science and Technology, 29(2), 335-41.
25. Zhang P, Gearhart D, Van Dyke M, Su D, Esterhuizen E, Tulu B (2019). Ground response to high horizontal stresses during longwall retreat and its implications for longwall headgate support. International journal of mining science and technology, 29(1), 27-33.
26. Darvishi A, Ataei M, Rafiee R (2020). Investigating the effect of simultaneous extraction of two longwall panels on a maingate gateroad stability using numerical modeling. International Journal of Rock Mechanics and Mining Sciences, 126, 104172.
27. Shao L, Huang B, Zhao X. Secondary Gob-side Entry Retaining Technology with Double Side Roof Cutting and Pressure Relief in Thin Coal Seam. International Journal of Oil, Gas and Coal Engineering. 2020;8(5):91-102.
28. Guangchao Z, Chuanwei Z, Miao C, Guangzhe T, You L, Weihua H, et al (2021). Ground response of entries driven adjacent to a retreating longwall panel. International Journal of Rock Mechanics and Mining Sciences, 138, 104630.
29. Abbasi F, Khosravi MH, Jafari A, Bashari A, Alipenhani B (2021). Support Analysis of Main Tunnels in Tabas Mechanized Parvadeh Mine at Intersection with Coal Seam. Journal of Mining and Environment, 12(3), 711-24.
30. Tuncay D, Tulu IB, Klemetti T (2021). Investigating different methods used for approximating pillar loads in longwall coal mines. International Journal of Mining Science and Technology, 31(1), 23-32.
31. Ardehjani, E. A., Rafiee, R., & Ataei, M. (2021). The effect of the seam slopes on the strata behavior in the longwall coal mines using numerical modeling.
32. Eremin M, Peryshkin A, Esterhuizen G, Pavlova L, Fryanov V (2022). Numerical analysis of pillar stability in longwall mining of two adjacent panels of an inclined coal seam. Applied Sciences,12(21), 11028.
33. Zhang Z, Li Z, Xu G, Gao X, Liu Q, Li Z, et al (2023). Lateral abutment pressure distribution and evolution in wide pillars under the first mining effect. International Journal of Mining Science and Technology, 33(3), 309-22.
34. Bednarek Ł, Małkowski P, Niedbalski Z, Mucha K (2024). Steel arch and rock bolt support in terms of the Gateroad stability maintaining behind the longwall face. Applied Sciences, 14(9), 3594.
35. Yetkin ME, Ozfirat MK, Onargan T (2024). Examining the optimum panel pillar dimension in longwall mining considering stress distribution. Scientific Reports, 14(1), 6928.
36. Ansari E, Rafiee R, Ataei M (2024). Investigating Effect of Induced Stresses due to Coal Panel Extraction on Next Panel Strata behavior during Mechanized Longwall Mining: a Case Study. Journal of Mining and Environment, 15(1), 381-99.
37. Shekarchizadeh M, Najafi M, Fatehi Marji M (2025). Numerical Simulation of Appropriate Design for Selecting Tunnel Support Systems in Squeezing Grounds (Tunnel No. 2 in Tabas Coal Mine, Iran). Advances in Civil Engineering, (1), 4398231.
38. Sakurai S (1997). Lessons learned from field measurements in tunnelling. Tunnelling and underground space technology, 12(4), 453-60.
39. Ghasemzadeh, H., Madani, H., Sereshki, F., & Afraei, S. (2026). A new Model for Predicting Spontaneous Combustion of Coal Potential based on Decision Tree. Journal of Mining and Environment, 17(1), 333-349.
40. Tabas Coal Mine Technical Office (2005). Tabas coal mine project basic design report-mining.

ACCEPTED MANUSCRIPT

41. Itasca, F. (2013). Fast lagrangian analysis of continua in 3 dimensions. Online manual, 175-180.
42. Salamon, M. D. G. (2020). Mechanism of caving in longwall coal mining. In Rock mechanics contributions and challenges (pp. 161-168). CRC Press.

ACCEPTED MANUSCRIPT